



Supplementary Materials for
Close-range remote sensing of Saturn's rings during Cassini's ring-grazing orbits and Grand Finale

Matthew S. Tiscareno*, Philip D. Nicholson, Jeffrey N. Cuzzi, Linda J. Spilker, Carl D. Murray, Matthew M. Hedman, Joshua E. Colwell, Joseph A. Burns, Shawn M. Brooks, Roger N. Clark, Nicholas J. Cooper, Estelle Deau, Cecile Ferrari, Gianrico Filacchione, Richard G. Jerousek, Stéphane Le Mouélic, Ryuji Morishima, Stu Pilorz, Sébastien Rodriguez, Mark R. Showalter, Sarah V. Badman, Emily J. Baker, Bonnie J. Buratti, Kevin H. Baines, Christophe Sotin

*Corresponding author. Email: matt@seti.org

Published 14 June 2019, *Science* **364**, eaau1017 (2019)
DOI: 10.1126/science.aau1017

This PDF file includes:

Materials and Methods
Supplementary Text
Figs. S1 to S11
Tables S1 to S4
References

Materials and Methods

Observation details

Dates with form YYYY-DDD are in day-of-year (DOY) format, in which days are numbered sequentially rather than being cited by month. Observation times are given in Coordinated Universal Time (UTC).

ISS images were calibrated using the CISSCAL software package (5), which is available from the NASA Planetary Data System at <https://pds-rings.seti.org/cassini/iss/software.html>

The ISS instrument had two components, a Narrow Angle Camera (NAC) and a Wide Angle Camera (WAC).

The color mosaic shown in Fig. 1a was created by combining images from the Rev 257 DAPHNIS observation. Colors obtained at lower resolution were overlaid onto higher-resolution black-and-white images. The colors derive from the IR3, Green, and UV3 filters on Cassini's ISS camera, so Fig. 1a is not a true-color image but rather enhanced color.

Observation details for the remainder of Fig. 1 are as follows: (b) Image N1863268347, at 0.16 km px^{-1} . (c) A portion of image N1871322544, at 0.39 km px^{-1} . (d) A portion of image N1870702753, at 0.50 km px^{-1} . (e) A portion of image N1868838859, at 0.67 km px^{-1} .

Observation details for Fig. 2 are as follows: (a) Image N1870075955, at 0.52 km px^{-1} . (b) Image N1870076370, at 0.47 km px^{-1} . (c) Image N1866983227, at 0.41 km px^{-1} . (d) Image N1862643689, at 0.63 km px^{-1} . (e) Image N1875233884, at 0.33 km px^{-1} .

Figs. 3a through 3d have resolution $\sim 1.05 \text{ km px}^{-1}$ in the radial direction, while Fig. 3e has resolution $\sim 1.60 \text{ km px}^{-1}$ in the radial direction. The context mosaic (Fig. 3a) covers 4° of longitude ($\sim 10,000 \text{ km}$) and is composed of 13 ISS NAC images obtained on 2017 July 13. The radial width is 200 km.

The images in Fig. 4a are from the HRESCOLBC mosaic taken by the Cassini Imaging Science Subsystem (ISS) during Rev 282, on 2017-187 (July 6, 2017), with phase angle $\alpha = 109^\circ$, solar elevation angle $B' = 26.7^\circ$, and spacecraft elevation angle $B = 35^\circ$. The middle panel of Fig. 4a is a near-true-color set, constructed from Cassini's Red, Green, and Blue filters.

Figure 4b shows a three-color composite from the observation RADCOLOR, taken during Rev 00A on 2004-298 (October 24, 2004). The radial resolution at the ring ansa is 13 km px^{-1} . The phase angle $\alpha = 48^\circ$, solar elevation angle $B' = -23.6^\circ$, and spacecraft elevation angle $B = -7.5^\circ$, looking at the lit face. The specific images used were N1477310577(RED), N1477310627(GRN), and N1477310544 (BL1). The images were calibrated and geometrically corrected with the standard CISSCAL code to I/F , converted to tiff format, and aligned by hand as (respectively) RGB channels in Photoshop, with subsequent adjustments made to accentuate relative color contrast.

In Fig. 5, the false-color coding is red = $2.02 \mu\text{m}$, green = $1.78 \mu\text{m}$ and blue = $1.27 \mu\text{m}$. Further details are as follows: (a) This image from Rev 262 is 935 by 64 pixels in size, with an average radial spacing in the horizontal direction of 76 km. The data were acquired at a spacecraft elevation angle of $B \sim 71^\circ$ and a fixed phase angle of $\alpha = 62^\circ$. The local hour angle varied from ~ 10 to ~ 12 h. (c) This image from Rev 287 is 708 by 64 pixels in size, with an average radial spacing between vertical lines of 95 km. The data were acquired at a spacecraft elevation angle of $B \sim 80^\circ$ and a fixed phase angle of $\alpha = 73^\circ$. The local hour angle ranged from ~ 3 h in the A ring, at the start of the scan, to ~ 6 h in the C ring at its end.

The data in Fig. 6a have been rebinned to a uniform sampling resolution of 20 km. The data in Fig. 6b have been smoothed to a resolution of 100 km. The context profile in Fig. 6c has been binned to 10 km resolution.

Processing and modelling for images of the main rings

A radial profile can be derived from an image by azimuthally averaging pixels that fall within radial bins (11, 63). For Figs. 2, S3, and S4, a radial profile was combined with the geometry of the image to create a filter that was then subtracted from the image to obtain a version emphasizing azimuthal and compact structures. This radially filtered image is shown below the unfiltered image (included for context).

The 41 propellers identified in image N1871322544 (Fig. 1c) were fitted to a pair of offset two-dimensional gaussians according to a model that has been described previously (15). Results are listed in Table S1 and plotted in Fig. S1. The center of the model structure is given in terms of both image coordinates (line and sample, which are respectively the vertical and horizontal coordinates in pixels, as measured from the image’s top-left corner) and the radius and longitude within the ring plane. The azimuthal and radial dimensions of the fitted two-dimensional gaussians are a and b , respectively. The azimuthal and radial offsets between the centers of the fitted two-dimensional gaussians are $\Delta\ell$ and Δr , respectively.

Processing and modelling for images of the F ring

The mosaics in Figs. 3a through 3d are derived from the observation HIRESAFRG001 in Rev 283, obtained on 2017 July 13. The original sequence consisted of 81 NAC images using clear filters, each with an exposure duration of 1.2 s, covering 24.7° degrees of co-rotating longitude (based on an F ring mean motion of $581.96^\circ/\text{d}$ with an epoch of 2007 January 1 at 12:00 UTC). The mean longitudinal coverage of each image was 0.43° . Each image was reprojected with respect to an F ring core model (85, *their Table 3, Fit 11*). The final scale was $0.003^\circ \text{ px}^{-1}$ in longitude and 1 km px^{-1} in radius. The mosaic in Fig. 3a was cropped to show only the region between co-rotating longitudes 271.5° at the left and 275.5° at the right, covering 13 images. The radial extent is 200 km centered on the approximate location of the core and increasing in radius from the planet in the vertical direction. In Fig. 3a the faint ring

above the core and almost parallel to it is a sheared jet resulting from a collision elsewhere in the core. There is another, fainter sheared jet below the core and angled to it, meeting the core at approximately the location of the disturbed region shown in Fig. 3b. There is longitudinal smearing of 1 – 2 pixels in this mosaic.

Fig. 3b is an enlargement of a region ($\sim 0.67^\circ$ by 100 km) to the left of the main mosaic with a selected, inset enhancement highlighting a longitudinal feature $\sim 0.05^\circ$ (~ 100 km) in extent located ~ 55 km below the core, interpreted to contain a set of objects that have just collided with the F ring core. The enhancement also shows evidence of faint material connecting these objects to the core region. This is similar to previously observed structures (35) and complex mini-jets (34).

Fig. 3c is an enlargement of a section ($\sim 0.67^\circ$ by 100 km) of the core to the right of center. It shows a prominent mini-jet extending ~ 10 km from the outer edge of the core. The mini-jet itself seems to originate from a narrow ring component that appears to be parallel to the core but ~ 10 km closer to the planet. Left of the mini-jet is evidence for a faint fan structure extending over $\sim 0.3^\circ$ indicative of the presence of an embedded object on an orbit with a relative eccentricity with respect to the core (35, *their Fig. 3*; 86, *their Fig. 13.29*).

Fig. 3d is an enhanced enlargement of a section ($\sim 0.83^\circ$ by 60 km) at the right side of the mosaic. As with Fig. 3c, there is some evidence of a narrow component parallel to the core but below it. Several mini-jets protruding from the outer edge of the core extend by radial distances from the core edge ranging from ~ 7 km (at the left) to ~ 14 km (at the right). The mini-jets themselves may originate at the location of the narrow component, located ~ 10 km from the core closer to the planet. We interpret the objects forming the synchronised mini-jets to be made from loose agglomerations of material brought together under the perturbing effect of Prometheus (87). Prometheus and collisions with the core can also play a role in disrupting these objects but, to a first approximation, the disrupted pieces will maintain orbits close to their

original ones with perhaps small changes in semi-major axis leading to the constituent particles drifting with respect to one another. This in turn leads to the appearance of objects following similar trajectories as they cross the core.

Fig. 3e is an enhanced enlargement of a section ($\sim 0.83^\circ$ by 60 km) produced from images in the same observation, HIRESAFRG001 in Rev 283, but taken ~ 85 min after the mosaic shown in Figs. 3a through 3d. The full mosaic consisted of 41 NAC ISS images covering approximately the same range of co-rotating longitude. The mean longitudinal coverage of each image was 0.66° . A subset of 9 images covering co-rotating longitudes between 271.5° and 275.5° was taken and then a section of that was then used for a direct comparison with the core shown in Fig. 3d. Although the resolution is worse (1.60 km/pixel in the radial direction compared with 1.05 km px^{-1} in the original) it is sufficient to see that the same mini-jets can be identified and their orbital evolution observed. All mini-jet features have approximately doubled in length and undergone keplerian shear making them lean towards the left (lower co-rotating longitudes). The calculated velocities of $\sim 1.4 \text{ m s}^{-1}$ are consistent with those of the previously-described mini-jets (34). A similar lengthening and shearing process is seen to occur to the prominent mini-jet originally seen in Fig. 3c. It is not possible to resolve the narrow ring component in any section of the later mosaic.

The velocities of the mini-jets in the radial direction were calculated by measuring the radial distances covered in the 85-minute time interval between the detections shown in Figs. 3d and 3e, each of which consists of a radial reprojection. This provides no information about azimuthal velocities.

Monte Carlo models of scattering in closely-packed rings

We have made a preliminary assessment as to which of the various possibilities is the most plausible cause of the correlation of ring color with local optical depth, which is observed all the

way down to the resolution limit of a few km (Fig. 4a). To do this, we have used Monte Carlo ray tracing models of nonclassical, closely-spaced particles with realistic size distributions. This technique has been described previously (40, 73). It has been tested thoroughly against classical results in the limit where they should be valid, namely low optical depth and volume density (45). It has also been validated against published models (73) in the nonclassical regime of high optical depth and volume density, where there is no closed-form solution. Rather than assuming an isotropic (Lambertian) phase function as in previous work, we employ a particle roughness/shadowing parameter S , which parameterizes the phase function and albedo of the particles. The operation of this parameter has been described previously (76). Fig. S6 shows that, for the viewing geometry of Fig. 4a, multiple scattering increases with optical depth and with particle reflectance, for all values of S .

Fig. S6 shows the ratio $R_{I/F}$ of total ring I/F (that is, reflectivity) to the single scattering component,

$$R_{I/F} = \frac{(I/F)_{\text{total}}}{(I/F)_{\text{ss}}} \quad (\text{S1})$$

where $(I/F)_{\text{total}}$ is the total ring I/F and $(I/F)_{\text{ss}}$ is the single-scattering component of the I/F , for four different values of S . The multiple scattering contribution is thus $(R_{I/F} - 1)$ times as large as the singly-scattered contribution. This is all we need for a preliminary assessment, since Fig. S6 shows that all particle roughnesses share a common qualitative behavior. At this moderately high phase angle, the figure shows the multiple scattering contribution increasing dramatically with increasing normal reflectance of the particle surfaces; the effect is also stronger at higher optical depths. The effect of local volume density D is smaller than the optical depth or particle reflectance effects. This shows the importance of multiple scattering for optical depths in the range found in the observed part of the rings, in this illumination and viewing geometry. Since the individual particles are reddish (40, 43), the reflectance is higher at long wavelengths, so the multiple scattering contribution is also higher at long wavelengths

and optical-depth dependent (the $\tau = 3$ curves are higher than $\tau = 1$ curves). That is to say, at high particle reflectance, the ring brightness is optical depth dependent. However, at short wavelengths the particle reflectance is known to be low (40, 43); in this regime there is little or no optical depth dependence of ring brightness. The consequence is that the rings become more red as optical depth increases, at this part of the rings and in this geometry. This explains the observations more naturally than other possible explanations.

Observations and modelling for UVIS occultations

The streaks seen in high-resolution ISS images of Plateau P1 are elongated and aligned to the direction of orbital motion. In order to better understand this texture, we analyzed all 31 of the Cassini UVIS stellar occultations with $B < 35^\circ$. For an occultation, the angle of the observer's line of sight with respect to the ring plane is equal to both the stellar elevation angle B' and the spacecraft elevation angle B . In our data set, B ranges from 1.2° to 32.1° . The clock angle ϕ for these occultations, which is the orientation of the star's projected track on the ring plane with respect to the radial direction, ranged from $\phi = 3^\circ - 316^\circ$. We compared the normal optical depth τ_n measured by these occultations to those computed using a self-gravity wake model (88, 89). This model treats the ring as consisting of alternating regions of high and low optical depth aligned to the direction of orbital motion ($\phi = 90^\circ$) as seen in the ISS images. We constrain the gap optical depth to be no greater than 0.01, based on the dark appearance of the streaks on both the lit and unlit faces of the ring. The 31 optical depth profiles were binned to 10 km radial resolution to give average optical depths spanning many clumps and gaps at each viewing geometry. We modeled the ring using infinitely-long rectangular slabs separated by nearly empty gaps and found the best-fitting parameters by ray-tracing through the model ring and matching optical depths. Model computed optical depths fit well with a reduced chi-squared less than a homogenous ring model.

Derivation of ring temperatures

We excluded CIRS spectra with ratio of the angular displacement of the boresight during the signal integration to the angular size of the footprint > 0.5 , to avoid smeared data. To increase the signal-to-noise ratio, 10 nearby spectra were averaged for each pointing. The loss of the spatial resolution due to the averaging process remains small, because the radial extent of 10 nearby pointings is smaller than each footprint size in most cases. The ring spectrum I_ν as a function of wave number ν is assumed to take the form of

$$I_\nu = \beta B_\nu(T), \quad (\text{S2})$$

where β is a scaling factor incorporating the filling factor and the effective emissivity of the ring structure (Fig. S7), $B_\nu(T)$ is the wavenumber-dependent Planck function, and T is the representative ring temperature. The temperature T and the scaling factor β are simultaneously derived by minimizing χ^2 (80). The spectral data between 50 and 450 cm^{-1} (200 μm to 22 μm , which covers the blackbody peaks for all temperatures likely to occur within Saturn's rings) are used for the fitting. To see correlation/anti-correlation of ring temperatures with ring optical depth, a standard radial optical depth profile (a UVIS-measured occultation of the star β Centauri, (8)) was smoothed over the typical CIRS FP1 footprint size (84).

The observational geometries of radial scans are summarized in Table S2. For the C ring, the B ring, and the Cassini division, we use the radial scans (L262 and U262) taken on 2017-052 for both the lit and unlit sides. For the A ring, we use the radial scans (L268 and U268) taken on DOY 95 in 2017 for both the lit and unlit sides. The scans L268 and U268, although they cover only outer main rings, have spatial resolutions higher than those for L262 and U262 by a factor of ~ 2 . The observational geometries of two scans are similar to each other for each side of rings. Since the ring opening angles during these observations were very close to the maximum value given by the obliquity of Saturn, 26.73° , the ring temperature at each

observational geometry (e.g. phase angle) was also near a maximum for the mission.

Observation design and data processing for VIMS images

Observation design: Observations were made of the sunlit rings on RGO Revs 255 and 262 and on GF Rev 287, in each case starting at ~ 4 h before periapse (P) and ending at $P - 1$ h. The unlit side of the rings was observed on RGO Revs 260 and 262, starting at $P + 1$ h and continuing for 2.5 hrs. In each case, the instrument stared in a fixed inertial direction while the motion of the spacecraft carried the field of view across the rings, resulting in a single, continuous image (referred to as a ‘noodle’). The viewing direction was within 20° of normal to the ring plane for all five observations, in contrast to the relatively low values of B of the SOI observations (41), yielding a phase angle of $\alpha \sim 65^\circ$ for the sunlit rings and $\sim 130^\circ$ for the unlit rings. Table S4 lists the relevant geometric and instrumental parameters for each observation.

On Rev 262, the aim point moved outwards from the inner edge of the C ring to the F ring, as the range from Cassini to the rings decreased from 236,000 km to 111,000 km. VIMS was operated in its IR-high-resolution mode (90) with a corresponding radial resolution that varies from 116 km px^{-1} in the inner C ring to 62 km px^{-1} at the F ring. Simultaneous observations were obtained with the VIMS Visible channel (VIS), operating in its nominal (or low-resolution) mode with a radial resolution that varies from 120 to 60 km px^{-1} .

On Rev 287, the aim point moved inwards from the F ring to the C ring, with the range to the rings decreasing from 194,000 km to 117,000 km. The corresponding IR radial resolution varies from 79 km px^{-1} in the outer A ring to 52 km px^{-1} in the inner C ring. Simultaneous observations were obtained with VIS, this time operating in its high-resolution mode with a radial resolution that steadily improves from 32 to 20 km px^{-1} .

A difference between the sunlit scans on Revs 262 and 287 is their azimuthal location relative to the sub-solar point on the rings: the former was made at an average solar hour angle (i.e.,

local time) of ~ 11 hrs, where saturnshine on the rings is a maximum, whereas the latter was obtained at ~ 4.5 hrs, with much less scattered light from the planet. This affects some features in the C ring spectra.

Although VIMS usually operates as an imaging spectrometer, it does this via an internal 2D scanning mirror (6). Typical frame times are several minutes, even for bright targets. In order to avoid the substantial distortion and smear that would have resulted from the rapidly-changing geometry near periapse on these orbits, the instrument was instead placed in LINE mode. In this whisk-broom mode, the scanning mirror moves in only 1 direction, producing a sequence of 64-pixel long lines painted on the target in a diagonal direction (91). As the instrument's boresight moved across the rings, the result was a single, very long, narrow image (a noodle) spanning the entire ring system.

For all lit-side observations, integration times were 160 ms per pixel for the IR channel and 5.1 s per line for the VIS channel and the scan-line length was 64 pixels. The interval between successive lines was 10.9 s, which together with the projected velocity of the aim point across the rings of $7\text{--}9 \text{ km s}^{-1}$, sets the radial interline spacing of 75–95 km in the noodles. Smear in the IR observations amounts to only ~ 1.3 km but for the visible channel it is ~ 40 km at an integration time of 5 sec per line, slightly larger than the VIS high-resolution pixel size.

With the exception of the scan on Rev 255, all observations were executed as planned and successfully returned data. On Rev 255, a problem at the Deep Space Network tracking station resulted in the central half of the scan, between the middle B ring and the inner A ring, being lost. We therefore only analyze the complete lit-side scans on Revs 262 and 287.

Image processing: In order to convert the raw line-mode data into color images such as those in Fig. 5, we followed the following steps. Individual lines were first converted to I/F spectra using the standard VIMS pipeline calibration procedure (92), modified to use a refined background correction specific to noodle mode. As described above, individual lines were then

assembled into a single noodle image with no geometric corrections or re-interpolation. A standard de-spiking algorithm was employed to remove charged-particle and γ -ray hits from Cassini's radioactive power units. A color composite version of the image was then created using wavelengths of 2.02 μm (red), 1.78 μm (green), and 1.27 μm (blue), chosen to emphasize the variations in the IR spectrum across the rings. The red channel corresponds to the center of a strong water ice absorption band, while the blue channel corresponds to a much weaker water ice band. The green channel is a continuum wavelength. Finally, a square-root histogram stretch was applied to the data in order to emphasize variations in the fainter parts of the rings, especially the inner C ring, at the expense of the bright B ring.

For the Rev 262 data, we inserted an additional filtering step using the Minimum Noise Fraction algorithm (93) in order to remove a linear trend in color across the rings; no such trend was seen in the Rev 287 data. This had the effect of removing a bluish tone in the C ring and making the two noodle images more similar in overall color.

Spectral processing: To produce the plots of spectral parameters in Fig. 6 and Figs. S9–S11, we again started with the raw line-mode data, background-subtracted to remove instrumental dark current and thermal background, and first applied the standard VIMS flux calibration (92) to convert the measured counts to ring reflectivity, expressed as I/F . A despiking algorithm was then applied to remove charged-particle hits. The calibrated observations were geometrically navigated using the appropriate Cassini SPICE kernels (94) to predict the locations of various standard ring features in the individual line-mode images, based on the feature radii of (95). After any necessary small adjustments were made to the predicted pointing, the radius of each pixel was calculated, taking into account a known offset of ~ 2 pixels between the pointing of the IR and VIS channels.

The I/F spectra for all pixels were then sorted by ring radius and grouped into a uniform set of bins at 20 km intervals, and eventually used to calculate an average spectrum for each

bin. With 3500 radial bins across 70,000 km and a total of 708 64-pixel lines across the rings, an average of ~ 12 pixels contributed to the final average spectrum for each bin. Selected small groups of spectral channels were then used to calculate band depths for each radial bin, focussing on the water ice bands at 1.55 and 2.0 μm and the spectral peak at 3.6 μm .

Water-ice band depths D_B are calculated using the standard formula (96):

$$D_B = 1 - \frac{S(\lambda_0)}{S(\text{ref})}, \quad (\text{S3})$$

where $S(\lambda_0)$ is the I/F at the bottom of the band and $S(\text{ref}) = [S(\lambda_1) + S(\lambda_2)]/2$ is an average of the I/F values at reference wavelengths on either side of the band. Typically, we use the mean of 3–6 adjacent spectral channels to evaluate $S(\lambda_i)$, while avoiding known ‘hot’ channels.

The strengths of the water ice bands measured here, including the height of the peak at 3.6 μm , are sensitive to both the level of non-icy contamination within the water ice grains and to the regolith grain size, either of which can affect the path length of photons through the water ice (97). The band depths can also be affected by inter-particle scattering, which is chiefly important at high phase angles because of the strongly-backscattering nature of the ring particles’ phase function (62).

The Visible channel data were processed in essentially the same manner, though the longer integration time means that these data are somewhat smeared in radius compared with the IR data (see above). In this wavelength region the derived spectral indicators are slopes rather than band depths. Following (57), we define the 0.35 – 0.55 μm slope (referred to by some authors as the blue slope) as

$$0.35 - 0.55 \mu\text{m slope} = 1 - \frac{S(0.35)}{S(0.55)}, \quad (\text{S4})$$

where $S(0.35)$ and $S(0.55)$ are the I/F values at 0.35 μm and 0.55 μm , respectively, as calculated from a linear fit to this spectral interval. We define the 0.55 – 0.85 μm slope (referred to

by some authors as the red slope) as

$$0.55 - 0.85 \mu\text{m slope} = \frac{S(0.85)}{S(0.55)} - 1, \quad (\text{S5})$$

where $S(0.55)$ and $S(0.85)$ are the fitted I/F values at $0.55 \mu\text{m}$ and $0.85 \mu\text{m}$, respectively. The $0.55 - 0.85 \mu\text{m}$ slopes are generally close to zero and show relatively little variability across the rings, so are omitted from Fig. S10

Supplementary Text

Interpretation and discussion for images of the main rings

It was previously known that several ring properties are altered not only within the largest density waves in Saturn's rings but also in the regions surrounding them (33, 51–53, 57). The occurrence of propellers is among these properties, as they are missing from the halo regions surrounding the strongest density waves (15).

We find that, for moderately-sized density waves such as Prometheus 9:8 (Figs. 1c and S1, Table S1), propellers are present not only in the regions surrounding the wave but also in the innermost and outermost portions of the wave itself, though they are missing from the central part of the wave. A straightforward interpretation is that there are processes in the central parts of density waves that either destroy propellers or make them less visible, and that these effects extend far beyond the wave itself for the strongest waves but do not even extend to the margins of the wave for moderately-sized waves.

Furthermore, the size distribution of the propellers is perturbed in the regions on the margins of the wave, where they are present.

The most diagnostic measure of propeller size is Δr , which has a linear relation to the size of the moonlet causing the propeller-shaped disturbance (23). This quantity is plotted in

Fig. S1c, for propellers identified in image N1871322544. In unperturbed ring regions within this image, the propeller population is dominated by values of Δr between 0.15 km and 0.4 km, with smaller numbers of propellers that are respectively larger and smaller than that range. This is especially true in the regions outward of 129,070 km, where larger numbers make the statistics more robust. However, in the innermost regions of the Prometheus 9:8 density wave, larger propellers are more numerous than medium-sized propellers, and smaller propellers are absent. Conversely, in the outermost regions of the same wave, smaller propellers are nearly as numerous as medium-sized propellers, and larger propellers are nearly absent.

Interpretation and discussion for UVIS occultations and related models

For Plateau P1 we find the height-to-wavelength ratio of the clumps to be $H/\lambda \sim 0.015$, an average width-to-wavelength ration of $W/\lambda \sim 0.039$, and an average optical depth of the gaps of $\tau_{\text{gap}} \sim 0.001$, where H is the vertical thickness of the ring, W is the average width of the gaps, S is the average separation of the gaps and $\lambda = W + S$ is the radial wavelength of the gap pattern. This model is in contrast with the self-gravity wake parameters of the A and B rings, where the narrow features are opaque clumps. This difference indicates that a different mechanism is creating the low optical depth regions, perhaps by perturbations from particularly massive ring particles (31). Model-derived optical depths which produced these best-fitting parameters and optical depths measured by the UVIS stellar occultations of Plateau P1 are compared in Fig. S5. Combining the best-fitting model parameters with the autocorrelation length in P1 from occultation optical depth profiles, $\lambda \sim 695$ m gives $S \sim 668$ m, $W \sim 27$ m, and $H \sim 11$ m.

Temperature difference between the lit and unlit sides

Figure S8 shows temperature variations across the ring plane as a function of optical depth. The lit-side temperature is greater than the unlit-side temperature for all points in the rings. The

temperature difference overall increases with optical depth, as little sunlight reaches the unlit side of optically thick rings.

The temperature differences between the lit and unlit sides of the inner A ring (from 122,000 km to 124,000 km from Saturn's center) are larger than those for the inner B ring (from 92,000 km to 99,000 km from Saturn's center) although the optical depths of these two regions are similar to each other. This regional difference has many possible causes, including the different particle size distributions, vertical dynamics, differences in Saturn heating, and differences in self-gravity wakes. Occultations of Cassini's radio signal, as measured from Earth, revealed that the size distribution of the inner A ring is narrower than that for the B1 ring (39). This means that small particles are more abundant in the latter region. Spins of small particles are expected to be fast (98). Fast rotators tend to reduce the temperature difference across the ring (84).

For optically thin rings (the C ring and the Cassini Division), the higher lit-side temperatures than the unlit-side temperatures could be caused by the fact that the phase angles for the lit side are lower than those for the unlit side. Models indicate that the phase dependence of temperature is dependent on particle spin, with small fast rotators tending to reduce the phase dependence (84). If so, then a higher abundance of small fast rotators in the C ring, compared to the Cassini Division, could account for the relatively smaller temperature differences in the C ring.

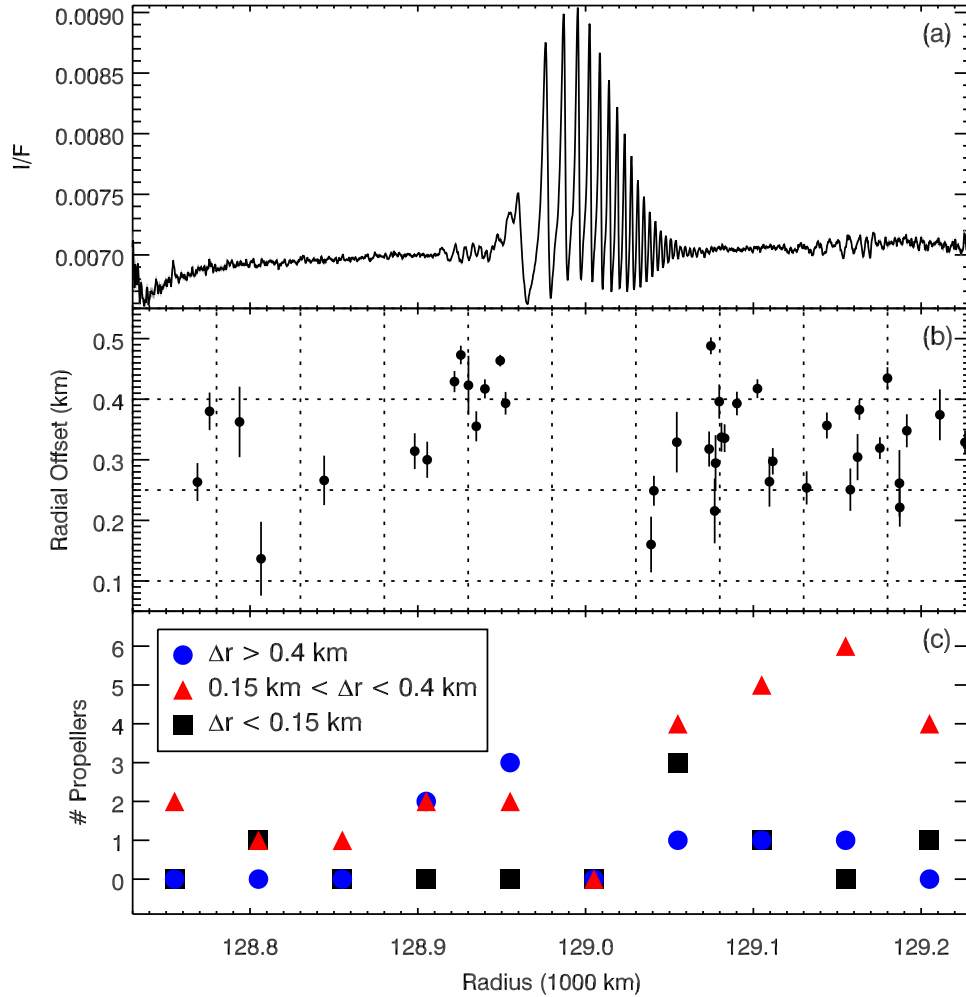


Figure S1: **Population statistics in the Propeller Belts.** (a) Radial profile of image N1871322544 (Fig. 1c), including the Prometheus 9:8 spiral density wave between approximately 128,940 and 129,070 km. (b) Size of propellers identified in image N1871322544, in terms of the radial offset Δr (Table S1). Dotted horizontal and vertical lines indicate the bins in size and location (respectively) used to generate the following plot. (c) Number of propellers belonging to each of three bins in size (see legend) at each bin in location.

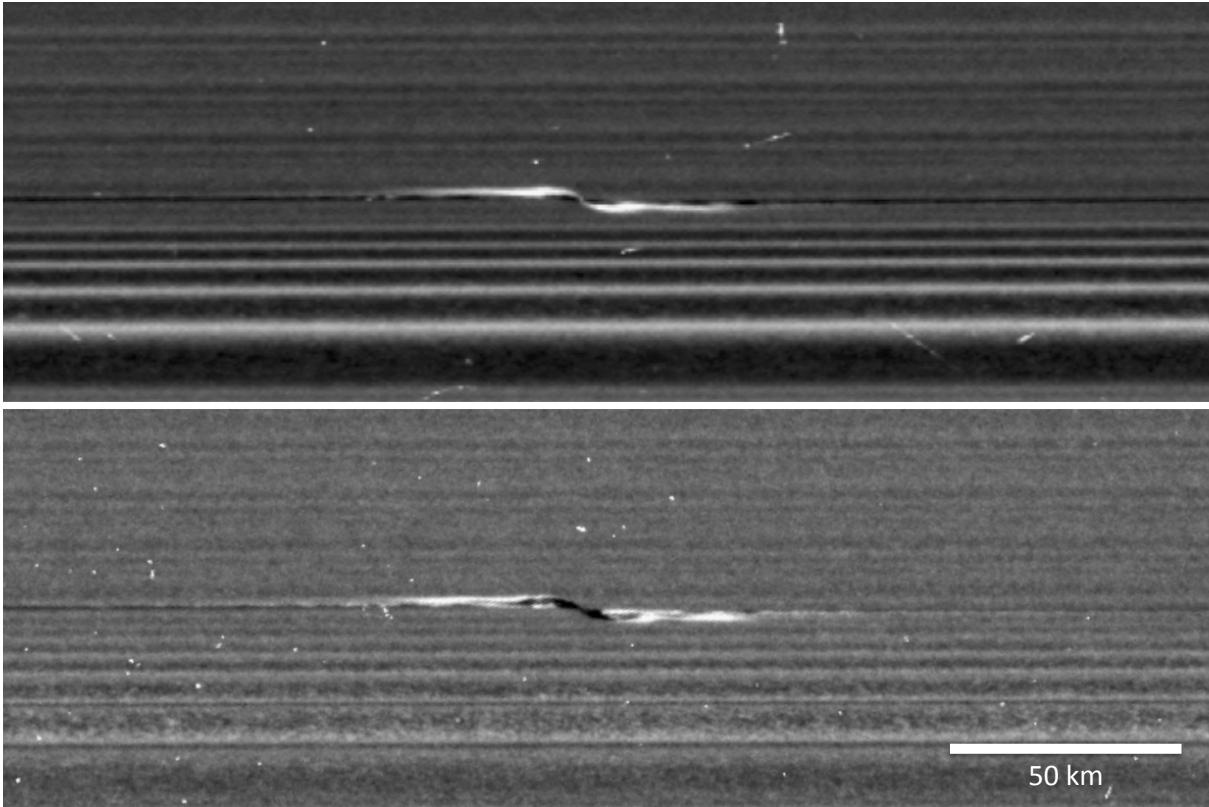


Figure S2: **Two sides of the same propeller.** Reprojected versions of images (a) N1866363047 and (b) N1866370342, showing the propeller Santos-Dumont on the lit and unlit sides of the rings, respectively. The unreprojected resolutions of the images are 0.53 and 0.41 km px^{-1} , respectively. They have been reprojected to the same resolution, for comparison.

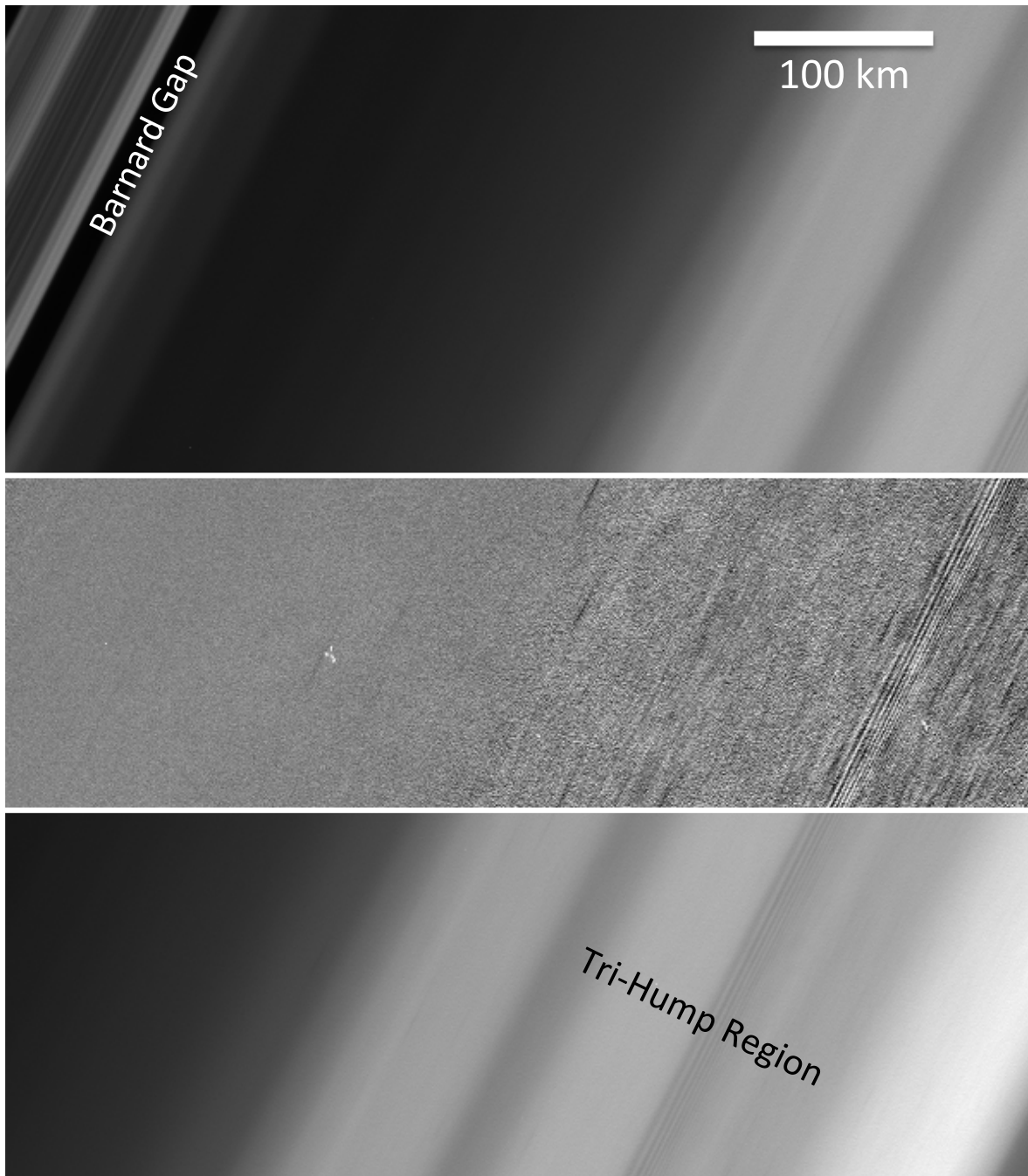


Figure S3: **Belts of textures in the outer Cassini Division.** A portion of image N1862642699, showing locations in the outer Cassini Division on the lit side of the rings at 0.69 km px^{-1} . As in Fig. 2, a strip through the middle has been filtered by subtracting the average radial profile of the image, so that local structures and textures are more visible.

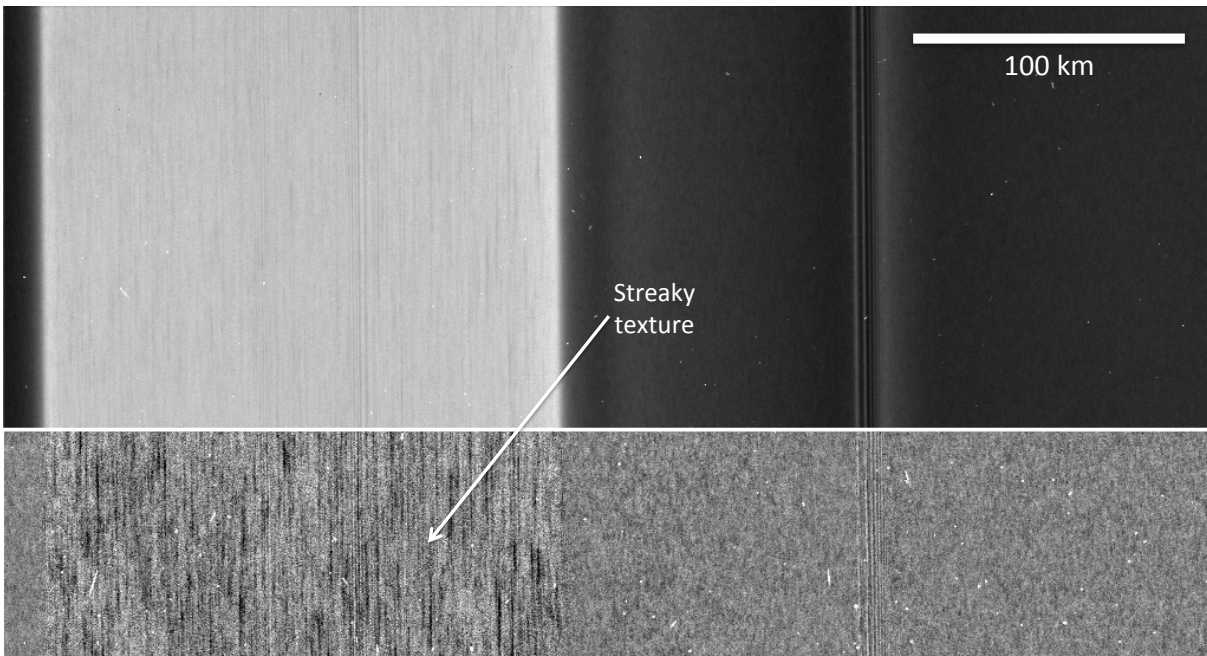


Figure S4: **Textures in the C ring.** A portion of image N1874678736, showing Plateau P5 in the C ring on the unlit side of the rings at 0.44 km px^{-1} . As in Fig. 2, a strip through the middle has been filtered by subtracting the average radial profile of the image, so that local structures and textures are more visible.

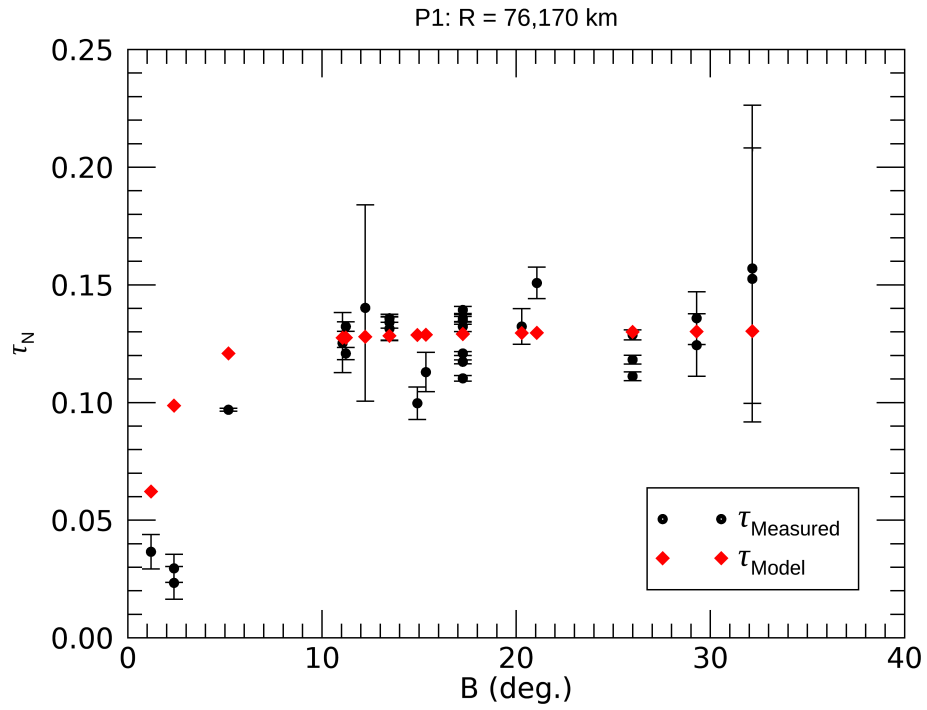


Figure S5: **Model-determined and measured UVIS normal optical depth in Plateau P1.** The results shown here minimize the reduced chi-squared statistic, $\chi^2 \sim 1.3$. The best-fitting model parameters are $H/\lambda \sim 0.015$, $W/\lambda \sim 0.039$, $\tau_{\text{gap}} \sim 0.001$, and $\tau_{\text{clump}} \sim 0.132$.

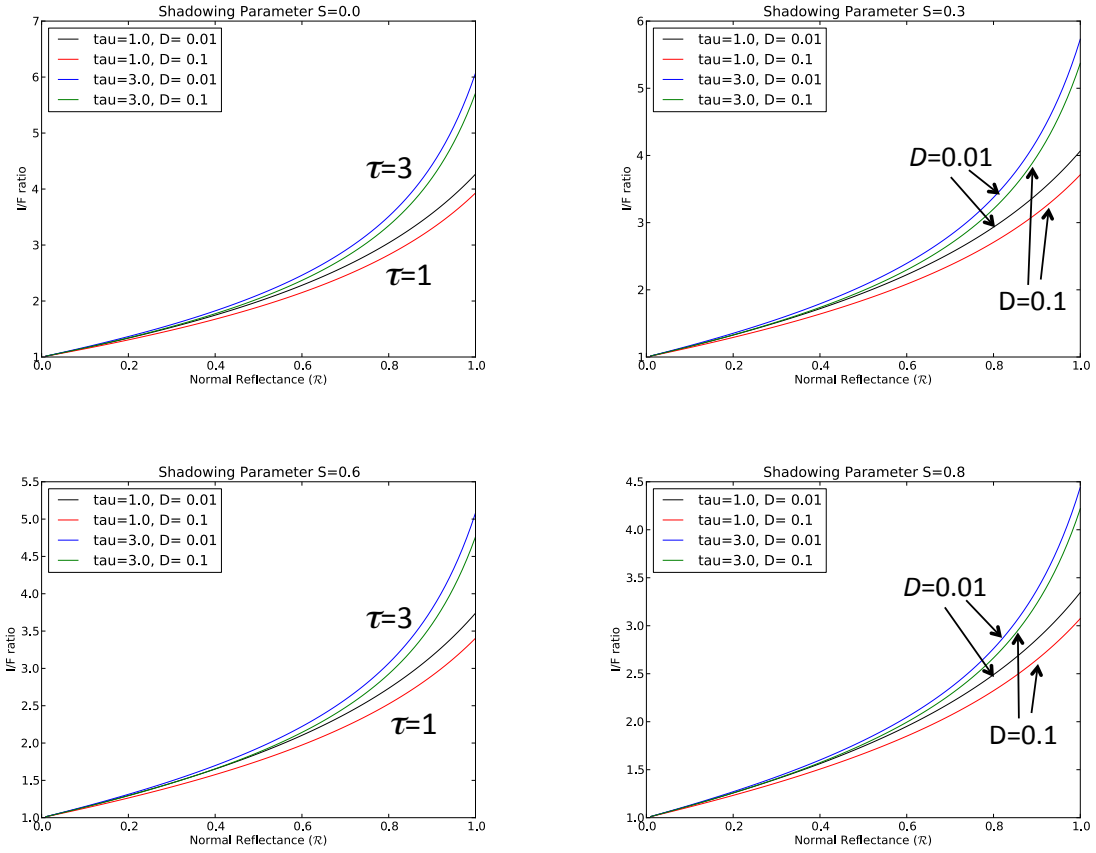


Figure S6: The four panels show the I/F ratio $R_{I/F}$, calculated at the illumination and viewing geometry of Fig. 4a (phase angle $\alpha = 111^\circ$, solar elevation angle $B' = 26^\circ$, spacecraft elevation angle $B = 41^\circ$). The normal reflectance on the horizontal coordinate (the angle-integrated reflectance of a smooth facet of the same surface material) is closely related to the particle spherical albedo (76). Each panel is for a different surface roughness/shadowing parameter S , where the ring particles are in the range of $S = 0.8$, depending on wavelength (43). The curves are labeled by their optical depth τ and particle volume density D .

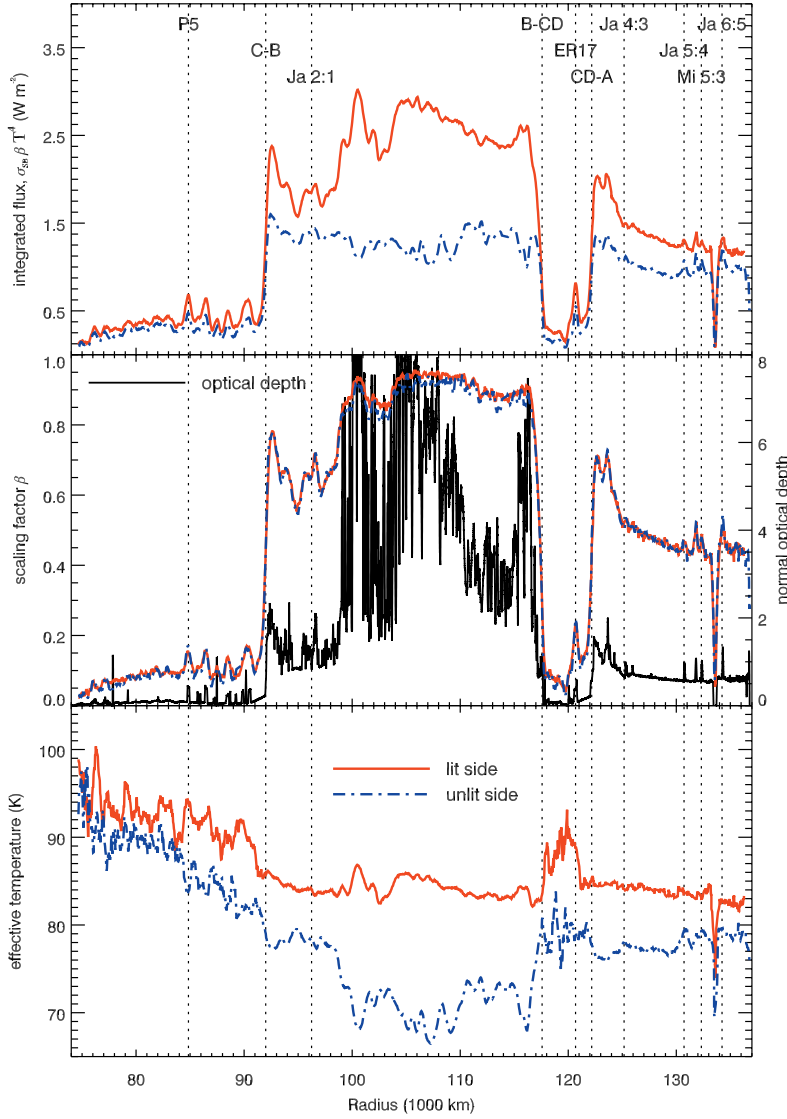


Figure S7: **Radial profiles of thermal infrared properties.** Data from the CIRS lit (red) and unlit-side (blue) scans on Rev 262. The upper panel shows the integrated flux $\sigma_{\text{SB}}\beta T^4$, where σ_{SB} is the Stefan-Boltzmann constant, with the vertical dotted lines indicating the locations of the ring boundaries, the strongest density waves, and two prominent features in the C ring and the Cassini Division (plateau P5 and the tri-hump region ER17). The middle panel shows the scaling factor β along with a normal optical depth profile obtained from a UVIS occultation of the star β Centauri on Rev 077, smoothed at a radial resolution of 10 km. The bottom panel shows the effective temperature T . β and T are simultaneously obtained from fitting the Planck function, see Eq. S2.

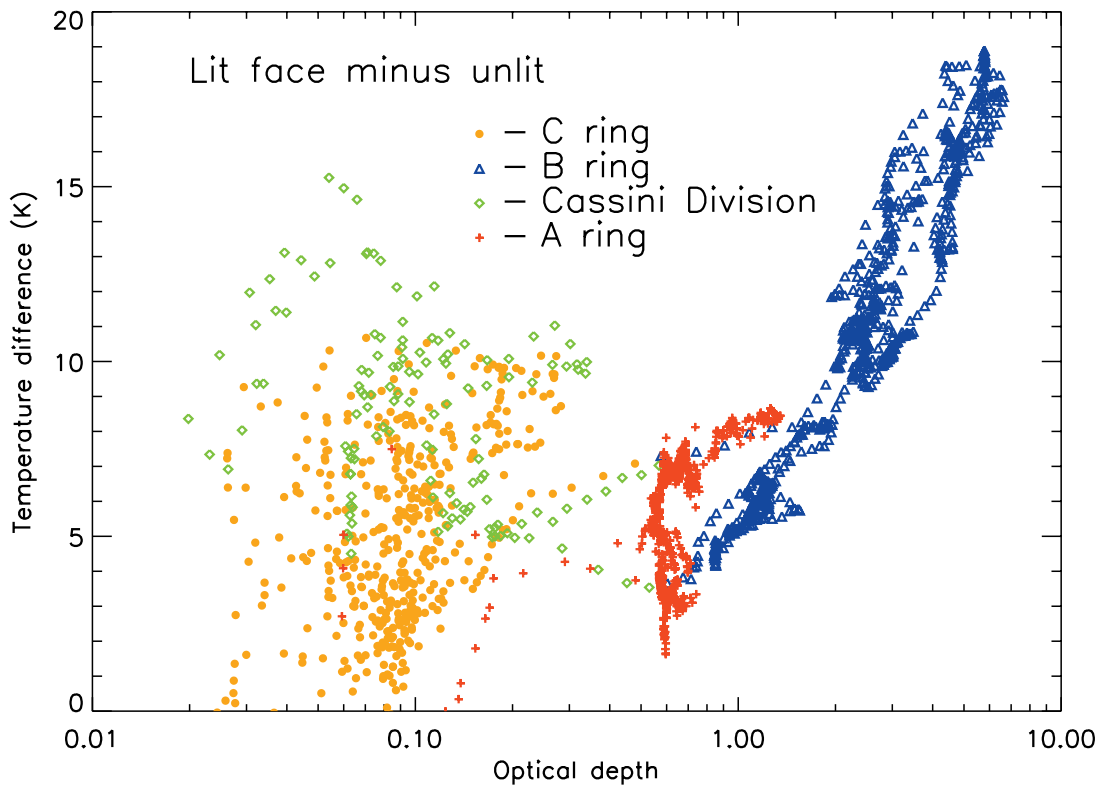


Figure S8: **Temperature difference across the ring plane.** Data plotted as a function of optical depth. Individual rings are identified by color: A ring in red (plus signs); B ring in blue (triangles); C ring in orange (filled circles); Cassini Division in green (diamonds).

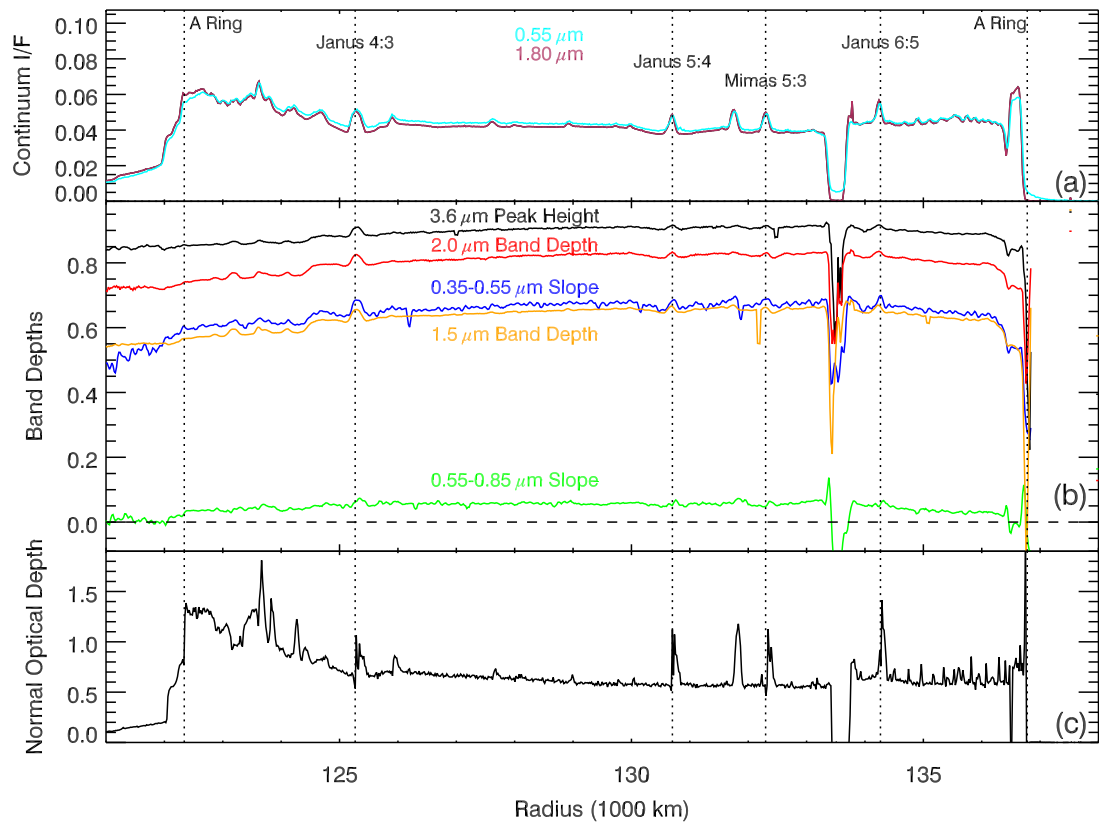


Figure S9: **Radial profiles of spectral parameters: A ring.** As in Fig. 6, but zoomed to show the vicinity of the A ring.

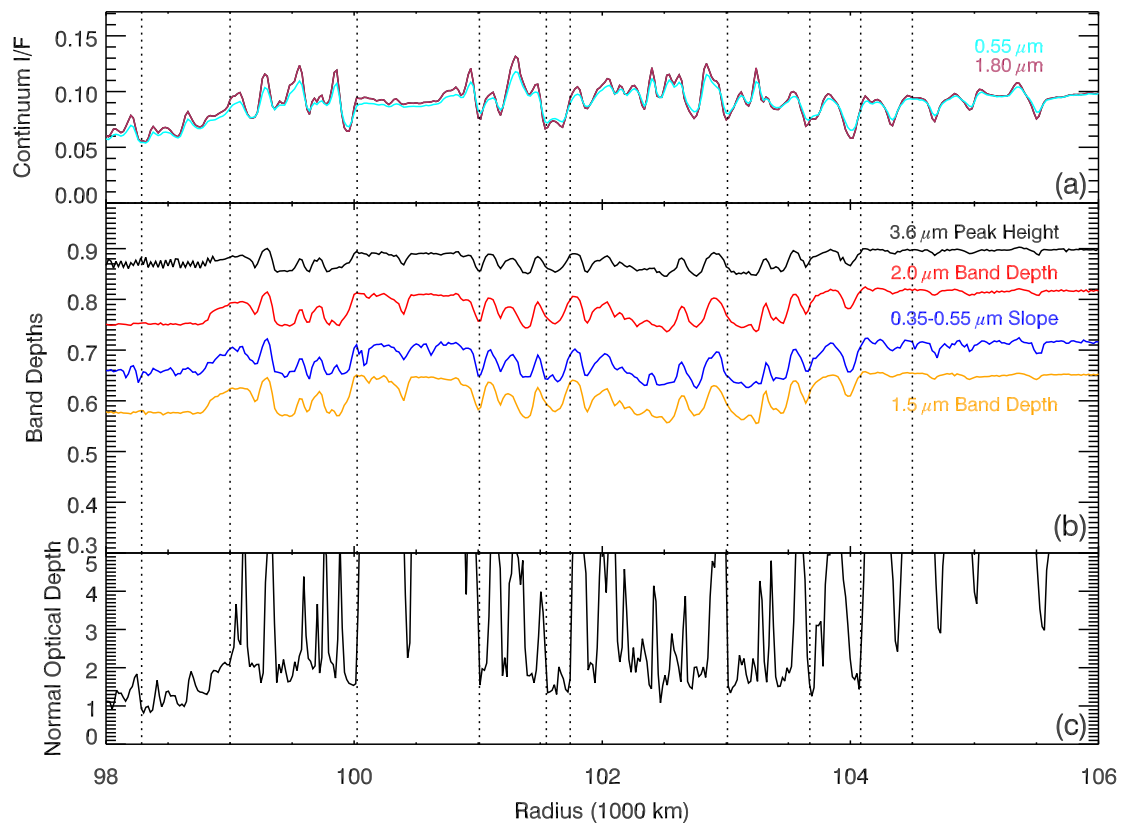


Figure S10: **Radial profiles of spectral parameters: B2 ring region.** As in Fig. 6, but zoomed to show the B2 region of the B ring (the same region covered in Fig. 4a). The green curve ($0.55 - 0.85 \mu\text{m}$ slope) is omitted because it is essentially zero and therefore off-scale.

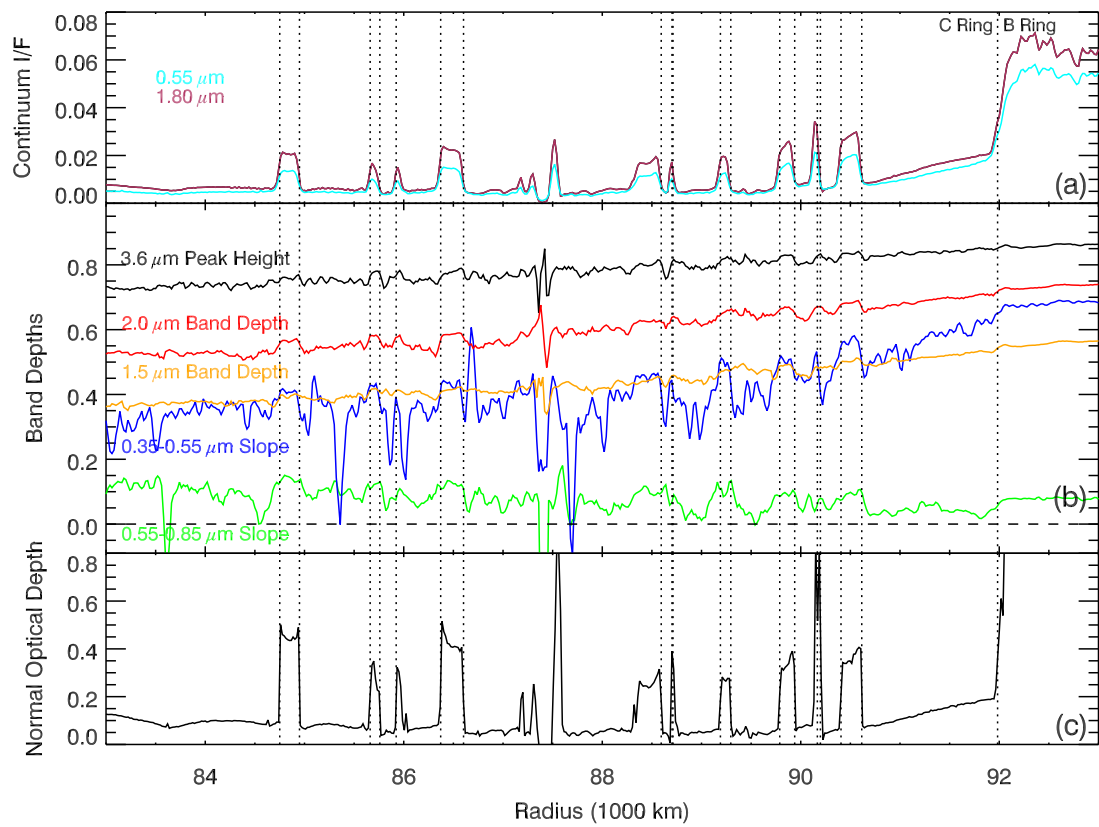


Figure S11: **Radial profiles of spectral parameters: outer C ring.** As in Fig. 6, but zoomed to show the vicinity of the outer C ring.

Table S1: Locations and fitted parameters for reported propellers. The format of Name is Orbit-Num-Letter, where Orbit and Num identify the image (in this case the image N1871322544, shown in Fig. 1c, is the 8th image of the high-resolution observation taken during Rev 270), and Letter identifies the feature within the image. Details of the model and parameters are as previously published (15). Selected parameters in this table are plotted in Fig. S1.

Name	Image	[line, sample]	Radius (km)	Longitude (°)	α (km)	b (km)	$\Delta\ell$ (km)	Δr (km)
270-008-A	N1871322544	[13.7, 944.4]	128952.31±0.39	344.39286±0.00017	1.570±0.043	0.628±0.020	3.090±0.046	0.393±0.019
270-008-B	"	[24.1, 261.0]	129175.40±0.39	344.33029±0.00017	1.607±0.043	0.601±0.016	3.010±0.044	0.319±0.018
270-008-C	"	[35.3, 100.1]	129226.14±0.39	344.31432±0.00017	1.878±0.054	0.607±0.019	3.317±0.056	0.329±0.019
270-008-D	"	[55.7, 478.5]	129097.53±0.39	344.34511±0.00018	0.876±0.062	0.790±0.062	-1.646±0.066	0.117±0.064
270-008-E	"	[60.8, 130.3]	129211.17±0.39	344.31331±0.00018	1.101±0.058	0.727±0.042	1.969±0.060	0.374±0.042
270-008-F	"	[61.0, 438.7]	129109.59±0.39	344.34079±0.00018	1.065±0.069	0.584±0.042	2.210±0.073	0.264±0.041
270-008-G	"	[64.9, 535.4]	129076.96±0.39	344.34886±0.00018	0.921±0.083	0.505±0.050	2.020±0.088	0.216±0.054
270-008-H	"	[81.3, 322.6]	129143.83±0.39	344.32749±0.00018	1.277±0.040	0.635±0.020	2.939±0.042	0.357±0.021
270-008-I	"	[85.0, 264.8]	129162.11±0.39	344.32181±0.00018	1.306±0.066	0.692±0.037	2.142±0.065	0.304±0.038
270-008-J	"	[94.0, 183.0]	129187.26±0.39	344.31320±0.00018	1.175±0.052	0.644±0.031	2.382±0.055	0.221±0.032
270-008-K	"	[102.2, 165.3]	129191.45±0.39	344.31044±0.00018	1.159±0.053	0.596±0.032	2.909±0.054	0.348±0.027
270-008-L	"	[161.8, 997.0]	128905.58±0.39	344.37608±0.00018	1.595±0.068	0.645±0.029	2.596±0.067	0.300±0.030
270-008-M	"	[168.6, 432.9]	129090.19±0.39	344.32468±0.00017	1.677±0.044	0.684±0.020	3.117±0.045	0.393±0.019
270-008-N	"	[175.6, 207.1]	129163.19±0.39	344.30353±0.00017	1.654±0.047	0.558±0.021	3.218±0.050	0.382±0.017
270-008-O	"	[219.2, 197.3]	129157.79±0.39	344.29635±0.00018	0.887±0.052	0.535±0.031	2.199±0.054	0.251±0.035
270-008-P	"	[224.4, 910.1]	128921.83±0.39	344.35923±0.00017	1.797±0.047	0.633±0.018	4.108±0.049	0.429±0.017
270-008-Q	"	[242.6, 887.6]	128925.65±0.39	344.35458±0.00017	2.209±0.050	0.625±0.014	4.095±0.051	0.473±0.015
270-008-R	"	[260.6, 960.1]	128898.18±0.39	344.35845±0.00018	1.366±0.060	0.607±0.027	2.301±0.060	0.314±0.030
270-008-S	"	[314.9, 218.9]	129131.76±0.39	344.28440±0.00018	1.164±0.050	0.586±0.027	2.452±0.053	0.254±0.027
270-008-T	"	[323.8, 367.7]	129080.99±0.39	344.29637±0.00018	1.595±0.058	0.590±0.021	3.311±0.061	0.337±0.024
270-008-U	"	[350.9, 286.4]	129102.43±0.39	344.28519±0.00017	1.774±0.041	0.626±0.016	3.495±0.043	0.417±0.016
270-008-V	"	[353.7, 372.0]	129073.64±0.39	344.29241±0.00018	1.153±0.050	0.606±0.030	2.327±0.053	0.318±0.029
270-008-W	"	[375.9, 14.4]	129187.07±0.39	344.25739±0.00018	1.044±0.089	0.582±0.056	1.929±0.093	0.261±0.055
270-008-X	"	[385.2, 788.2]	128930.16±0.39	344.32498±0.00018	1.222±0.083	0.667±0.051	2.160±0.085	0.423±0.049
270-008-Y	"	[396.0, 24.0]	129179.94±0.39	344.25532±0.00017	1.812±0.051	0.588±0.017	3.528±0.053	0.435±0.018
270-008-Z	"	[410.0, 320.0]	129079.66±0.39	344.27962±0.00018	1.679±0.076	0.623±0.031	3.265±0.073	0.396±0.028
270-008-a	"	[459.4, 413.6]	129039.02±0.39	344.28079±0.00018	1.223±0.073	0.774±0.043	1.681±0.061	0.160±0.046
270-008-b	"	[477.0, 286.4]	129077.48±0.39	344.26691±0.00018	0.867±0.060	0.625±0.049	1.924±0.063	0.295±0.046
270-008-c	"	[484.4, 714.5]	128934.83±0.39	344.30400±0.00018	1.528±0.059	0.586±0.022	2.490±0.058	0.355±0.025
270-008-d	"	[577.6, 642.9]	128940.00±0.39	344.28408±0.00017	1.706±0.037	0.669±0.016	3.280±0.038	0.417±0.016
270-008-e	"	[618.8, 313.0]	129040.70±0.39	344.24870±0.00018	1.492±0.054	0.612±0.026	2.889±0.057	0.249±0.025
270-008-f	"	[640.9, 84.8]	129111.57±0.39	344.22522±0.00017	1.997±0.059	0.684±0.021	3.194±0.057	0.298±0.022
270-008-g	"	[667.3, 993.6]	128806.56±0.39	344.30234±0.00018	0.961±0.088	0.592±0.056	1.576±0.087	0.137±0.061
270-008-h	"	[697.0, 861.8]	128844.17±0.39	344.28627±0.00018	1.395±0.080	0.647±0.040	2.284±0.080	0.266±0.041
270-008-i	"	[744.3, 515.5]	128949.11±0.39	344.24851±0.00017	2.359±0.033	0.619±0.009	4.457±0.034	0.464±0.010
270-008-j	"	[778.4, 114.4]	129074.69±0.39	344.20791±0.00017	2.079±0.044	0.625±0.013	3.344±0.043	0.488±0.014
270-008-k	"	[833.4, 932.9]	128793.74±0.39	344.27278±0.00018	1.002±0.097	0.583±0.056	1.668±0.090	0.363±0.058
270-008-l	"	[865.9, 123.7]	129054.37±0.39	344.19605±0.00018	1.200±0.073	0.747±0.048	1.960±0.072	0.329±0.050
270-008-m	"	[873.0, 985.3]	128768.63±0.39	344.27169±0.00018	1.715±0.072	0.681±0.029	2.735±0.070	0.263±0.031
270-008-n	"	[896.3, 19.2]	129082.84±0.39	344.18238±0.00018	1.943±0.068	0.598±0.022	3.186±0.068	0.336±0.023
270-008-o	"	[946.6, 919.4]	128775.86±0.39	344.25510±0.00018	1.361±0.055	0.701±0.032	2.352±0.056	0.380±0.031

Table S2: **Geometry data of CIRS radial scans.** Date is year and day of year, Rings is the rings covered by each scan, δa is the radial extent of the footprint projected on the ring plane, B' is the solar elevation angle, B is the spacecraft elevation angle, α is the phase angle, L is the local hour angle of ring particles around Saturn with the origin at the midnight, $L_{S/C}$ is the spacecraft local hour angle around the footprint, and $R_{S/C}$ is the spacecraft distance from the ring in units of Saturn's equatorial radius, R_{Sat} . All the values are mean values for each scan.

Scan	Date	Rings	δa (km)	B' (degs)	B (degs)	α (degs)	L (degs)	$L_{S/C}$ (degs)	$R_{S/C}$ (R_{Sat})
Lit face									
L262	2017-052	C, B, CD	795	26.70	71.09	62.06	179.64	98.65	3.39
L268	2017-095	A	363	26.72	78.86	56.00	182.23	140.22	1.63
Unlit face									
U262	2017-052	C, B, CD	632	26.70	-74.64	128.84	227.55	325.00	2.78
U268	2017-095	A	338	26.72	-82.89	120.95	212.27	260.51	1.47

Table S3: **Names of prominent features and their locations.** Widths are also shown for plateaux. The data for the plateaux are from (66). The data for the density waves are from (99). The location of the bending wave is from (100).

Name	location (km)	width (km)
P1	76188	155
P2	77085	150
P3	77378	65
P4	79243	45
P5	84850	200
P6	85708	95
P7	86490	230
P8	88473	245
P9	89865	105
P10	89863	150
P11	90508	205
ER17	120675	250
Janus 4:3 DW	125266	
Janus 5:4 DW	130700	
Mimas 5:3 BW	131898	
Mimas 5:3 DW	132295	
Janus 6:5 DW	134264	

Table S4: **List of VIMS ring spectral observations during the RGO and GF orbits.** Geometric data for VIMS radial scans. Obs_ID is the Cassini observation identifier. The date is given as year and day of year, Dur is the observation duration, including turns, and Range is the distance of Cassini from the ring target. B and α are the spacecraft elevation angle and phase angle at the observation point, which are constant across each scan. Dir'n specifies the direction of the scan across the rings: inwards or outwards, and H.A. is the (range of) local hour angles observed, where 0h = midnight and 12h = noon. v_{rad} is the projected velocity of the VIMS pixel across the rings, in the radial direction. Pixels indicates the length of each scan line, t_{line} the duration of a scan line, and Lines the total number of lines in the scan. Δr is the average radial spacing between successive lines.

Obs-ID	Date (year-day)	Dur. (h:mm)	Range (10^3 km)	B (deg)	α (deg)	Dir'n	H.A. (hr)	v_{rad} (km/s)	pixels	t_{line} (sec)	Lines	Δr (km)
VIMS-255RI-COMPLITB	2017-002	3:00	212-80	73	56	out	10-12	7.0	64	10.9	512	76
VIMS-260RI-COMPDRK	2017-038	2:30	111-209	74	129	in	~ 15	-7.0	32	5.7	1318	40
VIMS-262RI-COMPLITB	2017-052	3:00	236-111	71	62	out	10-12	7.0	64	10.9	935	76
VIMS-262RI-COMPDRK	2017-052	2:30	104-199	74	129	in	~ 14	-7.0	32	5.7	1483	40
VIMS-287RI-COMPLITB	2017-219	2:53	194-117	80	73	in	3-6	-8.9	64	10.9	708	95

References and Notes

1. J. N. Cuzzi, G. Filacchione, E. A. Marouf, *Planetary Ring Systems: Properties, Structure, and Evolution*, M. S. Tiscareno, C. D. Murray, Eds. (Cambridge Univ. Press, 2018), pp. 51–92.
2. Optical depth τ quantifies the attenuation of a beam of light passing through the disk, measured in e -folding terms. That is, $\tau \equiv -\ln \mathcal{T}$ for the fractional transparency \mathcal{T} . The normal optical depth τ_n corrects for the effects of an inclined line of sight, thus approximating what the optical depth would be if the line of sight were normal to the ring plane (that is, if observed face-on to the rings).
3. M. M. Hedman, F. Postberg, D. P. Hamilton, S. Renner, H.-W. Hsu, *Planetary Ring Systems: Properties, Structure, and Evolution*, M. S. Tiscareno, C. D. Murray, Eds. (Cambridge Univ. Press, 2018), pp. 308–337.
4. Materials and methods are available as supplementary materials.
5. C. C. Porco, R. A. West, S. Squyres, A. McEwen, P. Thomas, C. D. Murray, A. Delgenio, A. P. Ingersoll, T. V. Johnson, G. Neukum, J. Veverka, L. Dones, A. Brahic, J. A. Burns, V. Haemmerle, B. Knowles, D. Dawson, T. Roatsch, K. Beurle, W. Owen, Cassini imaging science: Instrument characteristics and anticipated scientific investigations at Saturn. *Space Sci. Rev.* **115**, 363–497 (2004). [doi:10.1007/s11214-004-1456-7](https://doi.org/10.1007/s11214-004-1456-7)
6. R. H. Brown, K. H. Baines, G. Bellucci, J.-P. Bibring, B. J. Buratti, F. Capaccioni, P. Cerroni, R. N. Clark, A. Coradini, D. P. Cruikshank, P. Drossart, V. Formisano, R. Jaumann, Y. Langevin, D. L. Matson, T. B. McCord, V. Mennella, E. Miller, R. M. Nelson, P. D. Nicholson, B. Sicardy, C. Sotin, The Cassini Visual and Infrared Mapping Spectrometer (Vims) Investigation. *Space Sci. Rev.* **115**, 111–168 (2004). [doi:10.1007/s11214-004-1453-x](https://doi.org/10.1007/s11214-004-1453-x)
7. F. M. Flasar, V. G. Kunde, M. M. Abbas, R. K. Achterberg, P. Ade, A. Barucci, B. B'ezard, G. L. Bjoraker, J. C. Brasunas, S. Calcutt, R. Carlson, C. J. C'esarsky, B. J. Conrath, A. Coradini, R. Courtin, A. Coustenis, S. Edberg, S. Edgington, C. Ferrari, T. Fouchet, D. Gautier, P. J. Gierasch, K. Grossman, P. Irwin, D. E. Jennings, E. Lellouch, A. A. Mamoutkine, A. Marten, J. P. Meyer, C. A. Nixon, G. S. Orton, T. C. Owen, J. C. Pearl, R. Prang'e, F. Raulin, P. L. Read, P. N. Romani, R. E. Samuelson, M. E. Segura, M. R. Showalter, A. A. Simon-Miller, M. D. Smith, J. R. Spencer, L. J. Spilker, F. W. Taylor, Exploring The Saturn System In The Thermal Infrared: The Composite Infrared Spectrometer. *Space Sci. Rev.* **115**, 169–297 (2004). [doi:10.1007/s11214-004-1454-9](https://doi.org/10.1007/s11214-004-1454-9)
8. J. E. Colwell, L. W. Esposito, R. G. Jerousek, M. Sremčević, D. Pettis, E. T. Bradley, Cassini UVIS stellar occultation observations of Saturn's rings. *Astron. J.* **140**, 1569–1578 (2010). [doi:10.1088/0004-6256/140/6/1569](https://doi.org/10.1088/0004-6256/140/6/1569)
9. P. Goldreich, S. Tremaine, The Dynamics of Planetary Rings. *Annu. Rev. Astron. Astrophys.* **20**, 249–283 (1982). [doi:10.1146/annurev.aa.20.090182.001341](https://doi.org/10.1146/annurev.aa.20.090182.001341)
10. F. H. Shu, *Planetary Rings*, R. Greenberg, A. Brahic, Eds. (Univ. of Arizona Press, Tucson, 1984), pp. 513–561.

11. M. S. Tiscareno, J. A. Burns, P. D. Nicholson, M. M. Hedman, C. C. Porco, Cassini imaging of Saturn's rings. *Icarus* **189**, 14–34 (2007). [doi:10.1016/j.icarus.2006.12.025](https://doi.org/10.1016/j.icarus.2006.12.025)
12. F. Spahn *et al.*, *Planetary Ring Systems: Properties, Structure, and Evolution*, M. S. Tiscareno, C. D. Murray, Eds. (Cambridge Univ. Press, 2018), pp. 157–197.
13. M. S. Tiscareno, J. A. Burns, M. M. Hedman, C. C. Porco, J. W. Weiss, L. Dones, D. C. Richardson, C. D. Murray, 100-metre-diameter moonlets in Saturn's A ring from observations of 'propeller' structures. *Nature* **440**, 648–650 (2006). [doi:10.1038/nature04581](https://doi.org/10.1038/nature04581) [Medline](#)
14. M. Sremčević, J. Schmidt, H. Salo, M. Seiss, F. Spahn, N. Albers, A belt of moonlets in Saturn's A ring. *Nature* **449**, 1019–1021 (2007). [doi:10.1038/nature06224](https://doi.org/10.1038/nature06224) [Medline](#)
15. M. S. Tiscareno, J. A. Burns, M. M. Hedman, C. C. Porco, The population of propellers in Saturn's A ring. *Astron. J.* **135**, 1083–1091 (2008). [doi:10.1088/0004-6256/135/3/1083](https://doi.org/10.1088/0004-6256/135/3/1083)
16. M. S. Tiscareno, J. A. Burns, M. Sremčević, K. Beurle, M. M. Hedman, N. J. Cooper, A. J. Milano, M. W. Evans, C. C. Porco, J. N. Spitale, J. W. Weiss, Physical characteristics and non-Keplerian orbital motion of "propeller" moons embedded in Saturn's rings. *Astrophys. J.* **718**, L92–L96 (2010). [doi:10.1088/2041-8205/718/2/L92](https://doi.org/10.1088/2041-8205/718/2/L92)
17. B. J. Buratti, P. C. Thomas, E. Roussos, C. Howett, M. Seiß, A. R. Hendrix, P. Helfenstein, R. H. Brown, R. N. Clark, T. Denk, G. Filacchione, H. Hoffmann, G. H. Jones, N. Khawaja, P. Kollmann, N. Krupp, J. Lunine, T. W. Momary, C. Paranicas, F. Postberg, M. Sachse, F. Spahn, J. Spencer, R. Srama, T. Albin, K. H. Baines, M. Ciarniello, T. Economou, H.-W. Hsu, S. Kempf, S. M. Krimigis, D. Mitchell, G. Moragas-Klostermeyer, P. D. Nicholson, C. C. Porco, H. Rosenberg, J. Simolka, L. A. Soderblom, Close Cassini flybys of Saturn's ring moons Pan, Daphnis, Atlas, Pandora, and Epimetheus. *Science* **364**, eaat2349 (2019).
18. Keplerian shear is the difference in orbital velocity between adjacent streamlines of ring material. For angular velocity n and radial distance a from Saturn's center, it is straightforward to differentiate Kepler's third law and obtain $dn/da = (3/2)(n/a)$.
19. J. W. Weiss, C. C. Porco, M. S. Tiscareno, Ring edge waves and the masses of nearby satellites. *Astron. J.* **138**, 272–286 (2009). [doi:10.1088/0004-6256/138/1/272](https://doi.org/10.1088/0004-6256/138/1/272)
20. M. S. Tiscareno *et al.*, *AAS Division for Planetary Sciences Meeting Abstracts* **37**, 64.02 (2005).
21. P. A. Torrey, M. S. Tiscareno, J. A. Burns, C. C. Porco, *AAS Division on Dynamical Astronomy Meeting Abstracts* **39**, 15.19 (2008).
22. R. Tajeddine, P. D. Nicholson, M. S. Tiscareno, M. M. Hedman, J. A. Burns, M. E. Moutamid, Dynamical phenomena at the inner edge of the Keeler gap. *Icarus* **289**, 80–93 (2017). [doi:10.1016/j.icarus.2017.02.002](https://doi.org/10.1016/j.icarus.2017.02.002)
23. M. Seiß, F. Spahn, M. Sremčević, H. Salo, Structures induced by small moonlets in Saturn's rings: Implications for the Cassini Mission. *Geophys. Res. Lett.* **32**, L11205 (2005). [doi:10.1029/2005GL022506](https://doi.org/10.1029/2005GL022506)

24. M. S. Tiscareno, M. M. Hedman, J. A. Burns, J. C. Castillo-Rogez, Compositions and origins of outer planet systems: insights from the Roche critical density. *Astrophys. J.* **765**, L28 (2013). [doi:10.1088/2041-8205/765/2/L28](https://doi.org/10.1088/2041-8205/765/2/L28)
25. C. C. Porco, E. Baker, J. Barbara, K. Beurle, A. Brahic, J. A. Burns, S. Charnoz, N. Cooper, D. D. Dawson, A. D. Del Genio, T. Denk, L. Dones, U. Dyudina, M. W. Evans, B. Giese, K. Grazier, P. Helfenstein, A. P. Ingersoll, R. A. Jacobson, T. V. Johnson, A. McEwen, C. D. Murray, G. Neukum, W. M. Owen, J. Perry, T. Roatsch, J. Spitale, S. Squyres, P. Thomas, M. Tiscareno, E. Turtle, A. R. Vasavada, J. Veverka, R. Wagner, R. West, Cassini Imaging Science: Initial results on Saturn's rings and small satellites. *Science* **307**, 1226–1236 (2005). [doi:10.1126/science.1108056](https://doi.org/10.1126/science.1108056) [Medline](#)
26. M. C. Lewis, G. R. Stewart, Expectations for Cassini observations of ring material with nearby moons. *Icarus* **178**, 124–143 (2005). [doi:10.1016/j.icarus.2005.04.009](https://doi.org/10.1016/j.icarus.2005.04.009)
27. M. S. Tiscareno, M. M. Hedman, J. A. Burns, J. W. Weiss, C. C. Porco, Probing the inner boundaries of Saturn's A ring with the Iapetus –1:0 nodal bending wave. *Icarus* **224**, 201–208 (2013). [doi:10.1016/j.icarus.2013.02.026](https://doi.org/10.1016/j.icarus.2013.02.026)
28. M. M. Hedman, P. D. Nicholson, Kronoseismology: using density waves in Saturn's C ring to probe the planet's interior. *Astron. J.* **146**, 12 (2013). [doi:10.1088/0004-6256/146/1/12](https://doi.org/10.1088/0004-6256/146/1/12)
29. Regolith is any layer of loose surface material.
30. E. Déau, L. Dones, M. I. Mishchenko, R. A. West, P. Helfenstein, M. M. Hedman, C. C. Porco, The opposition effect in Saturn's main rings as seen by Cassini ISS: 4. Correlations of the surge morphology with surface albedos and VIMS spectral properties. *Icarus* **305**, 324–349 (2018). [doi:10.1016/j.icarus.2017.12.025](https://doi.org/10.1016/j.icarus.2017.12.025)
31. K. Baillié, J. E. Colwell, L. W. Esposito, M. C. Lewis, Meter-sized moonlet population in Saturn's C ring and Cassini Dy. *Astron. J.* **145**, 171 (2013). [doi:10.1088/0004-6256/145/6/171](https://doi.org/10.1088/0004-6256/145/6/171)
32. M. M. Hedman, P. D. Nicholson, More Kronoseismology with Saturn's rings. *Mon. Not. R. Astron. Soc.* **444**, 1369–1388 (2014). [doi:10.1093/mnras/stu1503](https://doi.org/10.1093/mnras/stu1503)
33. J. E. Colwell, L. W. Esposito, J. H. Cooney, Particle sizes in Saturn's rings from UVIS stellar occultations 1. Variations with ring region. *Icarus* **300**, 150–166 (2018). [doi:10.1016/j.icarus.2017.08.036](https://doi.org/10.1016/j.icarus.2017.08.036)
34. N. O. Attree, C. D. Murray, G. A. Williams, N. J. Cooper, A survey of low-velocity collisional features in Saturn's F ring. *Icarus* **227**, 56–66 (2014). [doi:10.1016/j.icarus.2013.09.008](https://doi.org/10.1016/j.icarus.2013.09.008)
35. C. D. Murray, K. Beurle, N. J. Cooper, M. W. Evans, G. A. Williams, S. Charnoz, The determination of the structure of Saturn's F ring by nearby moonlets. *Nature* **453**, 739–744 (2008). [doi:10.1038/nature06999](https://doi.org/10.1038/nature06999) [Medline](#)
36. M. S. Tiscareno, C. J. Mitchell, C. D. Murray, D. Di Nino, M. M. Hedman, J. Schmidt, J. A. Burns, J. N. Cuzzi, C. C. Porco, K. Beurle, M. W. Evans, Observations of ejecta clouds produced by impacts onto Saturn's rings. *Science* **340**, 460–464 (2013). [doi:10.1126/science.1233524](https://doi.org/10.1126/science.1233524) [Medline](#)

37. M. M. Hedman, J. A. Burns, M. R. Showalter, Corrugations and eccentric spirals in Saturn's D ring: New insights into what happened at Saturn in 1983. *Icarus* **248**, 137–161 (2015). [doi:10.1016/j.icarus.2014.10.021](https://doi.org/10.1016/j.icarus.2014.10.021)
38. J. N. Cuzzi, A. D. Whizin, R. C. Hogan, A. R. Dobrovolskis, L. Dones, M. R. Showalter, J. E. Colwell, J. D. Scargle, Saturn's F Ring core: Calm in the midst of chaos. *Icarus* **232**, 157–175 (2014). [doi:10.1016/j.icarus.2013.12.027](https://doi.org/10.1016/j.icarus.2013.12.027)
39. J. Cuzzi *et al.*, *Saturn from Cassini-Huygens*, M. Dougherty, L. Esposito, S. M. Krimigis, Eds. (Springer, 2009), pp. 459–509.
40. M. Ciarniello, G. Filacchione, E. D'Aversa, F. Capaccioni, P. D. Nicholson, J. N. Cuzzi, R. N. Clark, M. M. Hedman, C. M. Dalle Ore, P. Cerroni, C. Plainaki, L. J. Spilker, Cassini-VIMS observations of Saturn's main rings: II. A spectrophotometric study by means of Monte Carlo ray-tracing and Hapke's theory. *Icarus* **317**, 242–265 (2019). [doi:10.1016/j.icarus.2018.07.010](https://doi.org/10.1016/j.icarus.2018.07.010)
41. F. Poulet, J. N. Cuzzi, The Composition of Saturn's Rings. *Icarus* **160**, 350–358 (2002). [doi:10.1006/icar.2002.6967](https://doi.org/10.1006/icar.2002.6967)
42. F. Poulet, D. P. Cruikshank, J. N. Cuzzi, T. L. Roush, R. G. French, Compositions of Saturn's rings A, B, and C from high resolution near-infrared spectroscopic observations. *Astron. Astrophys.* **412**, 305–316 (2003). [doi:10.1051/0004-6361:20031123](https://doi.org/10.1051/0004-6361:20031123)
43. J. N. Cuzzi, R. G. French, A. R. Hendrix, D. M. Olson, T. Roush, S. Vahidinia, HST-STIS spectra and the redness of Saturn's rings. *Icarus* **309**, 363–388 (2018). [doi:10.1016/j.icarus.2018.02.025](https://doi.org/10.1016/j.icarus.2018.02.025)
44. R. N. Clark, D. P. Cruikshank, R. Jaumann, R. H. Brown, K. Stephan, C. M. Dalle Ore, K. Eric Livo, N. Pearson, J. M. Curchin, T. M. Hoefen, B. J. Buratti, G. Filacchione, K. H. Baines, P. D. Nicholson, The surface composition of Iapetus: Mapping results from Cassini VIMS. *Icarus* **218**, 831–860 (2012). [doi:10.1016/j.icarus.2012.01.008](https://doi.org/10.1016/j.icarus.2012.01.008)
45. J. N. Cuzzi, P. R. Estrada, Compositional Evolution of Saturn's Rings Due to Meteoroid Bombardment. *Icarus* **132**, 1–35 (1998). [doi:10.1006/icar.1997.5863](https://doi.org/10.1006/icar.1997.5863)
46. E. A. Marouf, G. L. Tyler, H. A. Zebker, R. A. Simpson, V. R. Eshleman, Particle size distributions in Saturn's rings from voyager 1 radio occultation. *Icarus* **54**, 189–211 (1983). [doi:10.1016/0019-1035\(83\)90192-6](https://doi.org/10.1016/0019-1035(83)90192-6)
47. H. A. Zebker, E. A. Marouf, G. L. Tyler, Saturn's rings: Particle size distributions for thin layer models. *Icarus* **64**, 531–548 (1985). [doi:10.1016/0019-1035\(85\)90074-0](https://doi.org/10.1016/0019-1035(85)90074-0)
48. R. G. French, P. D. Nicholson, Saturn's Rings II Particle Sizes Inferred from Stellar Occultation Data. *Icarus* **145**, 502–523 (2000). [doi:10.1006/icar.2000.6357](https://doi.org/10.1006/icar.2000.6357)
49. R. A. Harbison, P. D. Nicholson, M. M. Hedman, The smallest particles in Saturn's A and C Rings. *Icarus* **226**, 1225–1240 (2013). [doi:10.1016/j.icarus.2013.08.015](https://doi.org/10.1016/j.icarus.2013.08.015)
50. T. M. Becker, J. E. Colwell, L. W. Esposito, A. D. Bratcher, Characterizing the particle size distribution of Saturn's A ring with Cassini UVIS occultation data. *Icarus* **279**, 20–35 (2016). [doi:10.1016/j.icarus.2015.11.001](https://doi.org/10.1016/j.icarus.2015.11.001)

51. P. D. Nicholson, M. M. Hedman, R. N. Clark, M. R. Showalter, D. P. Cruikshank, J. N. Cuzzi, G. Filacchione, F. Capaccioni, P. Cerroni, G. B. Hansen, B. Sicardy, P. Drossart, R. H. Brown, B. J. Buratti, K. H. Baines, A. Coradini, A close look at Saturn's rings with Cassini VIMS. *Icarus* **193**, 182–212 (2008). [doi:10.1016/j.icarus.2007.08.036](https://doi.org/10.1016/j.icarus.2007.08.036)
52. M. M. Hedman, P. D. Nicholson, J. N. Cuzzi, R. N. Clark, G. Filacchione, F. Capaccioni, M. Ciarniello, Connections between spectra and structure in Saturn's main rings based on Cassini VIMS data. *Icarus* **223**, 105–130 (2013). [doi:10.1016/j.icarus.2012.10.014](https://doi.org/10.1016/j.icarus.2012.10.014)
53. G. Filacchione, M. Ciarniello, F. Capaccioni, R. N. Clark, P. D. Nicholson, M. M. Hedman, J. N. Cuzzi, D. P. Cruikshank, C. M. Dalle Ore, R. H. Brown, P. Cerroni, N. Altobelli, L. J. Spilker, Cassini–VIMS observations of Saturn's main rings: I. Spectral properties and temperature radial profiles variability with phase angle and elevation. *Icarus* **241**, 45–65 (2014). [doi:10.1016/j.icarus.2014.06.001](https://doi.org/10.1016/j.icarus.2014.06.001)
54. J. N. Cuzzi, J. A. Burns, S. Charnoz, R. N. Clark, J. E. Colwell, L. Dones, L. W. Esposito, G. Filacchione, R. G. French, M. M. Hedman, S. Kempf, E. A. Marouf, C. D. Murray, P. D. Nicholson, C. C. Porco, J. Schmidt, M. R. Showalter, L. J. Spilker, J. N. Spitale, R. Srama, M. Sremcević, M. S. Tiscareno, J. Weiss, An evolving view of Saturn's dynamic rings. *Science* **327**, 1470–1475 (2010). [doi:10.1126/science.1179118](https://doi.org/10.1126/science.1179118) [Medline](#)
55. J. H. Waite Jr., R. S. Perryman, M. E. Perry, K. E. Miller, J. Bell, T. E. Cravens, C. R. Glein, J. Grimes, M. Hedman, J. Cuzzi, T. Brockwell, B. Teolis, L. Moore, D. G. Mitchell, A. Persoon, W. S. Kurth, J.-E. Wahlund, M. Morooka, L. Z. Hadid, S. Chocron, J. Walker, A. Nagy, R. Yelle, S. Ledvina, R. Johnson, W. Tseng, O. J. Tucker, W.-H. Ip, Chemical interactions between Saturn's atmosphere and its rings. *Science* **362**, eaat2382 (2018). [doi:10.1126/science.aat2382](https://doi.org/10.1126/science.aat2382) [Medline](#)
56. R. H. Brown, K. H. Baines, G. Bellucci, B. J. Buratti, F. Capaccioni, P. Cerroni, R. N. Clark, A. Coradini, D. P. Cruikshank, P. Drossart, V. Formisano, R. Jaumann, Y. Langevin, D. L. Matson, T. B. McCord, V. Mennella, R. M. Nelson, P. D. Nicholson, B. Sicardy, C. Sotin, N. Baugh, C. A. Griffith, G. B. Hansen, C. A. Hibbitts, T. W. Momary, M. R. Showalter, Observations in the Saturn system during approach and orbital insertion, with Cassini's visual and infrared mapping spectrometer (VIMS). *Astron. Astrophys.* **446**, 707–716 (2006). [doi:10.1051/0004-6361:20053054](https://doi.org/10.1051/0004-6361:20053054)
57. G. Filacchione, F. Capaccioni, M. Ciarniello, R. N. Clark, J. N. Cuzzi, P. D. Nicholson, D. P. Cruikshank, M. M. Hedman, B. J. Buratti, J. I. Lunine, L. A. Soderblom, F. Tosi, P. Cerroni, R. H. Brown, T. B. McCord, R. Jaumann, K. Stephan, K. H. Baines, E. Flamini, Saturn's icy satellites and rings investigated by Cassini–VIMS: III – Radial compositional variability. *Icarus* **220**, 1064–1096 (2012). [doi:10.1016/j.icarus.2012.06.040](https://doi.org/10.1016/j.icarus.2012.06.040)
58. The Rev code is a three-digit label for Cassini's orbits around Saturn. For operational reasons, Saturn orbit insertion (SOI) was followed by Revs 00A, 00B, and 00C, and then by Revs 003 through 293.
59. I/F is a measure of the observed brightness I as normalized by a perfect Lambert surface's reflection of the incident solar flux πF .

60. Z. Zhang, A. G. Hayes, M. A. Janssen, P. D. Nicholson, J. N. Cuzzi, I. de Pater, D. E. Dunn, P. R. Estrada, M. M. Hedman, Cassini microwave observations provide clues to the origin of Saturn's C ring. *Icarus* **281**, 297–321 (2017). [doi:10.1016/j.icarus.2016.07.020](https://doi.org/10.1016/j.icarus.2016.07.020)
61. The sharp peak at 123,570 km in both τ_n and I/F is probably associated with the Prometheus resonance.
62. L. Dones, J. N. Cuzzi, M. R. Showalter, Voyager Photometry of Saturn's A Ring. *Icarus* **105**, 184–215 (1993). [doi:10.1006/icar.1993.1118](https://doi.org/10.1006/icar.1993.1118)
63. M. S. Tiscareno, B. E. Harris, Mapping spiral waves and other radial features in Saturn's rings. *Icarus* **312**, 157–171 (2018). [doi:10.1016/j.icarus.2018.04.023](https://doi.org/10.1016/j.icarus.2018.04.023)
64. R. G. Jerousek, J. E. Colwell, L. W. Esposito, P. D. Nicholson, M. M. Hedman, Small particles and self-gravity wakes in Saturn's rings from UVIS and VIMS stellar occultations. *Icarus* **279**, 36–50 (2016). [doi:10.1016/j.icarus.2016.04.039](https://doi.org/10.1016/j.icarus.2016.04.039)
65. L. Iess, B. Militzer, Y. Kaspi, P. Nicholson, D. Durante, P. Racioppa, A. Anabtawi, E. Galanti, W. Hubbard, M. J. Mariani, P. Tortora, S. Wahl, M. Zannoni, Measurement and implications of Saturn's gravity field and ring mass. *Science* **364**, eaat2965 (2019).
66. J. E. Colwell *et al.*, *Saturn from Cassini-Huygens*, M. Dougherty, L. Esposito, S. M. Krimigis, Eds. (Springer, 2009), pp. 375–412.
67. L. J. Horn, J. N. Cuzzi, Characteristic Wavelengths of Irregular Structure in Saturn's B Ring. *Icarus* **119**, 285–310 (1996). [doi:10.1006/icar.1996.0021](https://doi.org/10.1006/icar.1996.0021)
68. P. R. Estrada, J. N. Cuzzi, Voyager Observations of the Color of Saturn's Rings. *Icarus* **122**, 251–272 (1996). [doi:10.1006/icar.1996.0124](https://doi.org/10.1006/icar.1996.0124)
69. P. R. Estrada, J. N. Cuzzi, M. R. Showalter, Voyager color photometry of Saturn's main rings: A correction. *Icarus* **166**, 212–222 (2003). [doi:10.1016/j.icarus.2003.06.001](https://doi.org/10.1016/j.icarus.2003.06.001)
70. M. M. Hedman, P. D. Nicholson, The B-ring's surface mass density from hidden density waves: Less than meets the eye? *Icarus* **279**, 109–124 (2016). [doi:10.1016/j.icarus.2016.01.007](https://doi.org/10.1016/j.icarus.2016.01.007)
71. P. R. Estrada, R. H. Durisen, J. N. Cuzzi, D. A. Morgan, Combined structural and compositional evolution of planetary rings due to micrometeoroid impacts and ballistic transport. *Icarus* **252**, 415–439 (2015). [doi:10.1016/j.icarus.2015.02.005](https://doi.org/10.1016/j.icarus.2015.02.005)
72. F. Poulet, J. N. Cuzzi, D. P. Cruikshank, T. Roush, C. M. Dalle Ore, Comparison between the Shkuratov and Hapke Scattering Theories for Solid Planetary Surfaces: Application to the Surface Composition of Two Centaurs. *Icarus* **160**, 313–324 (2002). [doi:10.1006/icar.2002.6970](https://doi.org/10.1006/icar.2002.6970)
73. H. Salo, R. G. French, The opposition and tilt effects of Saturn's rings from HST observations. *Icarus* **210**, 785–816 (2010). [doi:10.1016/j.icarus.2010.07.002](https://doi.org/10.1016/j.icarus.2010.07.002)
74. E. Déau, L. Dones, S. Charnoz, R. A. West, A. Brahic, J. Decriem, C. C. Porco, The opposition effect in Saturn's main rings as seen by Cassini ISS: 1. Morphology of phase functions and dependence on the local optical depth. *Icarus* **226**, 591–603 (2013). [doi:10.1016/j.icarus.2013.01.015](https://doi.org/10.1016/j.icarus.2013.01.015)

75. E. Déau, The opposition effect in Saturn's main rings as seen by Cassini ISS: 2. Constraints on the ring particles and their regolith with analytical radiative transfer models. *Icarus* **253**, 311–345 (2015). [doi:10.1016/j.icarus.2013.08.031](https://doi.org/10.1016/j.icarus.2013.08.031)
76. J. N. Cuzzi, L. B. Chambers, A. R. Hendrix, Rough surfaces: Is the dark stuff just shadow? *Icarus* **289**, 281–294 (2017). [doi:10.1016/j.icarus.2016.10.018](https://doi.org/10.1016/j.icarus.2016.10.018)
77. C. C. Porco, J. W. Weiss, D. C. Richardson, L. Dones, T. Quinn, H. Throop, Simulations of the dynamical and light-scattering behavior of Saturn's rings and the derivation of ring particle and disk properties. *Astron. J.* **136**, 2172–2200 (2008). [doi:10.1088/0004-6256/136/5/2172](https://doi.org/10.1088/0004-6256/136/5/2172)
78. V. G. Kunde *et al.*, in *Proc. SPIE Vol. 2803, Cassini/Huygens: A Mission to the Saturnian Systems*, L. Horn, Ed. (SPIE, 1996), pp. 162–177.
79. D. E. Jennings, F. M. Flasar, V. G. Kunde, C. A. Nixon, M. E. Segura, P. N. Romani, N. Gorius, S. Albright, J. C. Brasunas, R. C. Carlson, A. A. Mamoutkine, E. Guandique, M. S. Kaelberer, S. Aslam, R. K. Achterberg, G. L. Bjoraker, C. M. Anderson, V. Cottini, J. C. Pearl, M. D. Smith, B. E. Hesman, R. D. Barney, S. Calcutt, T. J. Vellacott, L. J. Spilker, S. G. Edgington, S. M. Brooks, P. Ade, P. J. Schinder, A. Coustenis, R. Courtin, G. Michel, R. Fettig, S. Pilorz, C. Ferrari, Composite infrared spectrometer (CIRS) on Cassini. *Appl. Opt.* **56**, 5274–5294 (2017). [doi:10.1364/AO.56.005274](https://doi.org/10.1364/AO.56.005274) [Medline](#)
80. L. J. Spilker, S. H. Pilorz, B. D. Wallis, J. C. Pearl, J. N. Cuzzi, S. M. Brooks, N. Altobelli, S. G. Edgington, M. Showalter, F. Michael Flasar, C. Ferrari, C. Leyrat, Cassini thermal observations of Saturn's main rings: Implications for particle rotation and vertical mixing. *Planet. Space Sci.* **54**, 1167–1176 (2006). [doi:10.1016/j.pss.2006.05.033](https://doi.org/10.1016/j.pss.2006.05.033)
81. L. Spilker, C. Ferrari, R. Morishima, Saturn's ring temperatures at equinox. *Icarus* **226**, 316–322 (2013). [doi:10.1016/j.icarus.2013.06.002](https://doi.org/10.1016/j.icarus.2013.06.002)
82. S. Pilorz, N. Altobelli, J. Colwell, M. Showalter, Thermal transport in Saturn's B ring inferred from Cassini CIRS. *Icarus* **254**, 157–177 (2015). [doi:10.1016/j.icarus.2015.01.002](https://doi.org/10.1016/j.icarus.2015.01.002)
83. E. Reffet, M. Verdier, C. Ferrari, Thickness of Saturn's B ring as derived from seasonal temperature variations measured by Cassini CIRS. *Icarus* **254**, 276–286 (2015). [doi:10.1016/j.icarus.2015.04.006](https://doi.org/10.1016/j.icarus.2015.04.006)
84. R. Morishima, L. Spilker, H. Salo, K. Ohtsuki, N. Altobelli, S. Pilortz, A multilayer model for thermal infrared emission of Saturn's rings II: Albedo, spins, and vertical mixing of ring particles inferred from Cassini CIRS. *Icarus* **210**, 330–345 (2010). [doi:10.1016/j.icarus.2010.06.032](https://doi.org/10.1016/j.icarus.2010.06.032)
85. N. J. Cooper, C. D. Murray, G. A. Williams, Local variability in the orbit of Saturn's F ring. *Astron. J.* **145**, 161 (2013). [doi:10.1088/0004-6256/145/6/161](https://doi.org/10.1088/0004-6256/145/6/161)
86. C. D. Murray, R. S. French, *Planetary Ring Systems: Properties, Structure, and Evolution*, M. S. Tiscareno, C. D. Murray, Eds. (Cambridge Univ. Press, 2018), pp. 338–362.
87. K. Beurle, C. D. Murray, G. A. Williams, M. W. Evans, N. J. Cooper, C. B. Agnor, Direct evidence for gravitational instability and moonlet formation in Saturn's rings. *Astrophys. J.* **718**, L176–L180 (2010). [doi:10.1088/2041-8205/718/2/L176](https://doi.org/10.1088/2041-8205/718/2/L176)

88. J. E. Colwell, L. W. Esposito, M. Sremčević, Self-gravity wakes in Saturn's A ring measured by stellar occultations from Cassini. *Geophys. Res. Lett.* **33**, L07201 (2006). [doi:10.1029/2005GL025163](https://doi.org/10.1029/2005GL025163)
89. J. E. Colwell, L. W. Esposito, M. Sremčević, G. R. Stewart, W. E. McClintock, Self-gravity wakes and radial structure of Saturn's B ring. *Icarus* **190**, 127–144 (2007). [doi:10.1016/j.icarus.2007.03.018](https://doi.org/10.1016/j.icarus.2007.03.018)
90. The standard VIMS instantaneous field of view (equivalent to a pixel for an optical imager) subtends a solid angle of 0.5×0.5 mrad. In IR-high-resolution mode, this is reduced to 0.25×0.5 mrad, with the smaller dimension in the VIMS fast-scan direction used in LINE mode.
91. This description applies to the instrument's IR channel, which employs a 1D detector array to obtain 256 simultaneous spectral measurements for each spatial pixel; the visible channel uses a charge-coupled device detector to obtain an entire line of pixels at 96 wavelengths simultaneously ("push-broom" mode). In LINE mode, the two channels are synchronized so that a full line of IR pixels is observed while the VIS channel does a single integration.
92. R. N. Clark, R. H. Brown, D. M. Lytle, M. Hedman, "The VIMS Wavelength and Radiometric Calibration 19, Final Report", *NASA Planetary Data System* (2018); https://atmos.nmsu.edu/data_and_services/atmospheres_data/Cassini/vims.html.
93. J. W. Boardman, F. A. Kruse, in *10th Thematic Conference on Geologic Remote Sensing* (Environmental Research Institute of Michigan, Ann Arbor, 1994), pp. 407–418.
94. C. H. Acton Jr., Ancillary data services of NASA's Navigation and Ancillary Information Facility. *Planet. Space Sci.* **44**, 65–70 (1996). [doi:10.1016/0032-0633\(95\)00107-7](https://doi.org/10.1016/0032-0633(95)00107-7)
95. R. G. French, P. D. Nicholson, M. L. Cooke, J. L. Elliot, K. Matthews, O. Perković, E. Tollestrup, P. Harvey, N. J. Chanover, M. A. Clark, E. W. Dunham, W. Forrest, J. Harrington, J. Pipher, A. Brahic, I. Grenier, F. Roques, M. Arndt, Geometry of the Saturn System from the 3 July 1989 Occultation of 28 Sgr and Voyager Observations. *Icarus* **103**, 163–214 (1993). [doi:10.1006/icar.1993.1066](https://doi.org/10.1006/icar.1993.1066)
96. R. N. Clark, T. L. Roush, Reflectance spectroscopy: Quantitative analysis techniques for remote sensing applications. *J. Geophys. Res.* **89**, 6329–6340 (1984). [doi:10.1029/JB089iB07p06329](https://doi.org/10.1029/JB089iB07p06329)
97. R. N. Clark, P. G. Lucey, Spectral properties of ice-particulate mixtures and implications for remote sensing: 1. Intimate mixtures. *J. Geophys. Res.* **89**, 6341–6348 (1984). [doi:10.1029/JB089iB07p06341](https://doi.org/10.1029/JB089iB07p06341)
98. R. Morishima, H. Salo, Simulations of dense planetary rings: IV. Spinning self-gravitating particles with size distribution. *Icarus* **181**, 272–291 (2006). [doi:10.1016/j.icarus.2005.10.023](https://doi.org/10.1016/j.icarus.2005.10.023)
99. L. J. Spilker, S. Pilorz, A. L. Lane, R. M. Nelson, B. Pollard, C. T. Russell, Saturn A ring surface mass densities from spiral density wave dispersion behavior. *Icarus* **171**, 372–390 (2004). [doi:10.1016/j.icarus.2004.05.016](https://doi.org/10.1016/j.icarus.2004.05.016)

100. D. L. Gresh, P. A. Rosen, G. L. Tyler, J. J. Lissauer, An analysis of bending waves in Saturn's rings using voyager radio occultation data. *Icarus* **68**, 481–502 (1986).
[doi:10.1016/0019-1035\(86\)90052-7](https://doi.org/10.1016/0019-1035(86)90052-7)